# THE DEEP GROTH STRIP SURVEY II. HUBBLE SPACE TELESCOPE STRUCTURAL PARAMETERS OF GALAXIES IN THE GROTH STRIP. $^{1,2}$

Luc Simard<sup>3,4</sup>, Christopher N. A. Willmer<sup>5</sup>, Nicole P. Vogt<sup>6</sup>, Vicki L. Sarajedini<sup>7</sup>, Andrew C. Phillips, Benjamin J. Weiner, David C. Koo, Myungshin Im<sup>8</sup>, Garth D. Illingworth, S. M. Faber

UCO/Lick Observatory, University of California, Santa Cruz, CA 95064, USA
Accepted for publication in ApJ Supplements, 16 April 2002

## ABSTRACT

The quantitative morphological classification of distant galaxies is essential to the understanding of the evolution of galaxies over the history of the Universe. This paper presents Hubble Space Telescope WFPC2 F606W and F814W photometric structural parameters for 7450 galaxies in the "Groth Strip." These parameters are based on a two-dimensional bulge+disk surface brightness model and were obtained using an automated reduction and analysis pipeline described in detail here. A first set of fits was performed separately in each bandpass, and a second set of fits was performed simultaneously on both bandpasses. The information produced by these two types of fits can be used to explore different science goals. Systematic and random fitting errors in all structural parameters as well as bulge and disk colors are carefully characterized through extensive sets of simulations. The results of these simulations are given in catalogs similar to the real science catalogs so that both real and simulated measurements can be sampled according to the same selection criteria to show biases and errors in the science data subset of interest. The effects of asymmetric structures on the recovered bulge+disk fitting parameters are also explored through simulations. The full multidimensional photometric survey selection function of the Groth Strip is also computed. This selection function, coupled to bias maps from simulations, provides a complete and objective reproduction of the observational limits, and these limits can be applied to theoretical predictions from galaxy evolution models for direct comparisons with the data.

Subject headings: galaxies: fundamental parameters, galaxies: evolution

## 1. INTRODUCTION

The visual classification of galaxies has a venerable tradition in optical astronomy starting with the introduction of Hubble's famous "Tuning Fork" diagram (Hubble 1936). Despite the fact that others have extended Hubble's original classification mainly to deal with the diversity of structures in later-type galaxies (de Vaucouleurs 1959; van den Bergh 1960a,b, 1976; Morgan 1970), the nomenclature of Hubble still very much pervades the language of today's galaxy morphology literature. This longevity is a tribute to Hubble's seminal work. However, visual classification has serious weaknesses. First and foremost, it is a subjective process. Although visual classification experts can agree to within two revised Hubble types (Naim et al. 1995), it is very difficult for non-experts to produce reliable visual classifications without years of hard-won experience. Second, it is also unclear how useful visual classification is with respect to high-redshift galaxies. Limited spatial resolution means that larger and larger internal galaxy structures such as spiral arms and tidal tails get progressively smoothed out with increasing redshift, and this smoothing can introduce significant classification biases.

No visual or quantitative classification system is perfect. However, provided a given quantitative system is clearly defined by its proponents, it is readily reproducible in its successes and failures by others. This is the fundamental advantage of the quantitative approach. Moreover, systematic and random errors of quantitative classifiers can be carefully characterized through extensive sets of galaxy image simulations covering a wide range of structural parameters. This is another important advantage. It should be emphasized that quantitative classification is meaningless without three important elements: the measurements themselves, the simulations and the galaxy selection function. This selection function is critical to relate observed structural parameter distributions to predictions from theoretical models.

A number of quantitative classifiers have been devel-

Based on observations made with the NASA/ESA Hubble Space Telescope which is operated by AURA, Inc., under contract with NASA.

<sup>&</sup>lt;sup>2</sup> Based on data obtained at the W.M. Keck Observatory, which is operated as a scientific partnership among the California Institute of Technology, the University of California and the National Aeronautics and Space Administration. The Observatory was made possible by the generous financial support of the W.M. Keck Foundation.

<sup>&</sup>lt;sup>3</sup> Guest User, Canadian Astronomy Data Center, which is operated by the National Research Council of Canada, Herzberg Institute of Astrophysics, Dominion Astrophysical Observatory

<sup>&</sup>lt;sup>4</sup> Current Address: Herzberg Institute of Astrophysics, National Research Council of Canada, 5071 West Saanich Road, Victoria, BC V9E 2E7, Canada

On leave from Observatorio Nacional, Rua General Jose Cristino 77, 20921-030 Sao Cristovao, RJ, Brazil

<sup>&</sup>lt;sup>6</sup> Current Address: Department of Astronomy, New Mexico State University, Las Cruces, NM 88003-8001, USA

<sup>&</sup>lt;sup>7</sup> Current Address: Department of Astronomy, University of Florida, Gainesville, FL 32611-2055, USA

<sup>8</sup> Current Address: SIRTF Science Center/IPAC, Mail Stop 220-6, California Institute of Technology, Pasadena, CA 91125, USA

oped/extended over the years to probe the structure of high-redshift galaxies. These classifiers can be either parametric (model-based) or non-parametric. Non-parametric classifiers include the C-A system (Watanabe et al. 1985; Abraham et al. 1994, 1996; Wu 1999; Conselice, Bershady, & Jangren 2000), artificial neural nets trained from visual classification sets (Odewahn 1995; Odewahn et al. 1996), and self-organizing maps (Naim et al. 1997). Parametric classifiers include radial multi-gaussian deconvolution (Bendinelli 1991; Fasano et al. 1998) and bulge+disk decomposition (Schade et al. 1995, 1996; Ratnatunga et al. 1999). The latter is popular for three reasons: (1) It is rooted in the very first studies of the functional form of galaxy radial surface brightness profiles (de Vaucouleurs 1948, 1959); (2) It provides a "comfortable" mental picture of the overall structure of a distant galaxy, i. e., it is conceptually simple to relate a quantitative measurement of galaxy type such as bulge-to-total light ratio to the familiar Hubble types; and (3) Photometric entities such as bulges and disks have distinct dynamical counterparts although this correspondence does not always hold (see Section 5.2 for more details).

This work uses GIM2D (Galaxy IMage 2D), a 2D decomposition fitting program (Simard 1998, and this paper), to measure the structural parameters of galaxies in the "Groth Strip" (Groth et al. 1994; Rhodes et al. 2000). GIM2D is an IRAF<sup>9</sup>/SPP package written to perform detailed bulge+disk surface brightness profile decompositions of low signal-to-noise (S/N) images of distant galaxies in a fully automated way. GIM2D takes an HST or ground-based science image and its source catalog, performs 2D profile fits on each source and produces modelsubtracted images as well as a full catalog of structural parameters. The bulge+disk model adopted here is not fundamentally new, but GIM2D offers an independent check of other galaxy classification works by including a set of extended features (Sérsic bulge profile, a comprehensive but by all means not exhaustive set of image asymmetry indices, three different fitting methods) and a different fitting algorithm. GIM2D has already been used in a variety of HST and ground-based distant galaxy studies: the optical structure of intermediate redshift compact narrowemission line galaxies (Guzmán et al. 1998), the quantitative morphology of Hubble Deep Field North galaxies (Marleau & Simard 1998), the NICMOS structure of a spiral galaxy lens at z = 0.4 (Maller et al. 2000), the luminosity-size relation of field disk galaxies from z = 0.1to z = 1.1 (Simard et al. 1999), the number density and luminosity function of E/SO galaxies to  $z \lesssim 1$  (Im et al. 2001), the Fundamental Plane of field absorption-line galaxies out to  $z \sim 1$  (Gebhardt et al. 2002), tests of hierarchical galaxy evolution models (Simard et al. 2002), the colors of luminous bulges at  $z \sim 1$  (Koo et al. 2002), the galaxy populations of poor, X-ray selected groups of galaxies (Tran et al. 2001) and of high and low X-ray luminosity galaxy clusters (Balogh et al. 2002), and the size evolution of high-redshift brightest cluster galaxies (Nelson et al. 2002).

This paper describes in detail the structural parameter analysis of galaxies in the Groth Strip from calibrated HST

archival images to final, parameter-rich structural catalogs for the entire Strip. It is a companion paper to Vogt et al. (2002) and Phillips et al. (2002) in which the spectroscopic Keck/Low Resolution Imaging Spectrograph survey of the Groth Strip undertaken by the Deep Extragalactic Evolutionary Probe (DEEP) team is described. Cosmological parameters adopted throughout this paper are  $H_0=70~{\rm km~s^{-1}~Mpc^{-1}}$ , and  $(\Omega_m, \Omega_\Lambda, \Omega_k)=(0.3, 0.7, 0.0)$ .

#### 2. OVERVIEW

Quantitative galaxy morphology classifiers must include three vital elements in order to be scientifically useful: the structural measurements themselves, extensive simulations, and a detailed survey selection function.

Every structural catalog should have a companion catalog of simulations from which the simulated counterparts of real data plots can be extracted. The ability to clearly visualize the systematic and random errors of a set of observed structural parameters is very helpful to quickly assess what science goals can be effectively pursued with the measurements. Morever, the systematic and random errors as characterized through these simulations can be applied to the theoretical predictions from galaxy evolution models to "scatter" the models in the same way as the observational errors would scatter signals from the real Universe

The survey selection function is constructed by inserting galaxy images with a wide range of input structural parameters into real images and calculating the success rate of the detection algorithm as a function of those parameters. This selection function serves two purposes: (1) It can be used to insure that studies of distant galaxies spanning a large range of redshifts treat galaxy samples at different redshifts in the same way (e.g., Simard et al. 1999). (2) The selection function can be used to "observe" theoretical models for a direct comparison with the data (e.g., Simard et al. 2002). Together with the simulations, the selection function provides the best possible way to reproduce the biases of the observational strategy.

Current and planned future on-line archival data systems contain (or will contain) prodigious amounts of data. Mining these systems in as automated a mode as possible holds the promise of fantastic scientific returns on problems requiring very large, statistically well-defined samples such as the evolution of galaxies. The automated GIM2D pipeline described in the next sections was designed to produce the above three elements with data mining of large datasets in mind.

The GIM2D pipeline includes the following steps: (1) Pre-processing, cosmic ray (CR) rejection and data quality mask creation (Section 3), (2) Source detection, deblending and extraction (Section 4), (3) Bulge+disk decompositions of galaxy images (Section 5) with a Point-Spread-Function (PSF) for each object (Section 5.1), (4) Creation of residual images and computation of residual image indices (Section 5.6), (5) Construction of measured structural parameter catalogs (Section 6), (6) Construction of associated catalogs of simulations for mapping systematic biases and random errors (Section 7), and (7) Construction of the survey selection function (Section 8).

<sup>&</sup>lt;sup>9</sup> IRAF is distributed by the National Optical Astronomy Observatories, which are operated by the Association of Universities for Research in Astronomy, Inc., under cooperative agreement with the National Science Foundation.

## 3. PRE-PROCESSING OF HST IMAGES

The GIM2D pipeline starts with the retrieval and preprocessing of HST archival images. Archival images are calibrated "on-the-fly" at retrieval time. The retrieved images are then sent through a set of IRAF scripts that removes cosmic rays and combine all the images taken in the same bandpass and at the same position on the sky together. The pipeline does not mosaic the three WFC chips together. Mosaicing (e. g., IRAF/STSDAS/WMOSAIC) destroys the uncorrelated noise characteristics of the original images by applying flux interpolations and geometric corrections. The noise characteristics of the science images must be preserved as much as possible through the whole pipeline so that it is possible to provide a realistic noise estimate to the likelihood function during the galaxy image fitting process. Each WFPC2 pointing is therefore split into three different images, one for each Wide-Field chip, and each chip is then processed independently through the rest of the pipeline. Each WFC chip covers a  $80'' \times 80''$  field of view with a pixel scale of 0".1/pixel. The Planetary Camera images were not analyzed since all the DEEP/GSS Keck spectroscopic targets were selected solely from the WFC images for the sake of sample homogeneity.

## 3.1. HST/WFPC2 Image Datasets

The HST images are from two surveys, collectively dubbed the "Groth Survey Strip" (GSS), taken under HST programs GTO 5090 (PI: Groth) and GTO 5109 (PI: Westphal). The GSS consists of 28 overlapping subfields taken with the HST Wide Field and Planetary Camera 2 (WFPC2) and forms a "chevron strip" oriented NE to SW at roughly 1417+52 at Galactic latitude  $b \sim 60^{\circ}$ . Each of 27 subfields has exposures of 2800 seconds ( $4 \times 700$  seconds) in the broad V filter (F606W) and 4400 seconds  $(4 \times 1100 \text{ seconds})$  in the broad I filter (F814W). The 28th field is the Westphal Deep Survey Field 2 (J2000 1417.5+52.5), with total exposures of 24,400 seconds in V and 25,200 seconds in I. The images were recalibrated "on-the-fly" through the Canadian Astronomy Data Center (CADC) standard pipeline (Pirenne et al. 1998). The datasets analyzed in this paper are listed in Table 1. Field 7 is the Westphal Deep Survey Field.

## 3.2. WFPC2 Data Quality Frames

Archival data produced through on-the-fly recalibration come in two parts: the science frames and the data quality frames (DQF). Each science frame comes with a data quality frame. This frame flags pixels in the science frame that have been corrupted for one reason or another (see Section 26.2.2 of HST Data Handbook Version 3.0 for DQF flag values). A DQF flag value of zero is used by the HST pipeline to flag good pixels. The GIM2D pipeline goes through the data quality frames of all science images in a given image stack<sup>10</sup> and identifies all the pixels with no good pixel values in the stack. The locations of these pixels are recorded and applied to the SExtractor segmentation image (Section 4.2) to make sure bad pixels are not included in the surface brightness fits.

#### 3.3. Cosmic Ray Rejection and Image Combination

The IRAF/STSDAS task CRREJ was used to reject cosmic rays from GSS WFPC2 image stacks. It combines a stack of consecutive exposures while eliminating cosmic rays and scaling the remaining pixels to the total exposure time of the stack. Cosmic rays are rejected through a series of sigma-clipping iterations. The number and sigma thresholds of these iterations are specified using the parameter SIGMAS. SIGMAS must be chosen carefully. If SIGMAS is too high, too many cosmic rays will be missed. On the other hand, if SIGMAS is too low, the CR rejection algorithm will start eating away at the noise in the background pixels. Unfortunately, there is no prescribed way of determining SIGMAS. The approach adopted here involved first the creation of a combined image with such high SIGMAS values that no pixels were rejected by CR-REJ. The resulting "HIGH" image showed all the cosmic rays that hit all the science images in the image stack. However, there were also plenty of untouched background pixels that showed what the background in the combined image should look like. CRREJ-combined images were then created with progressively lower values of SIGMAS, and blinked against the "HIGH" image. SIGMAS values were lowered until the noise in the untouched background areas of these images clearly showed they were being modified by the sigma-clipping with respect to the same areas in the "HIGH" image. The best value of SIGMAS was found to be "6,4" i. e., CRREJ was instructed to perform two sigma-clipping iterations, the first one at the  $6\sigma$ -level and the second one at the  $4\sigma$ -level. This value was then automatically applied in the combinations of all the GSS stacks. Even with the best SIGMAS cuts, a number of lowenergy cosmic rays will be left in the final combined image. If these low-energy cosmic rays significantly changed the background noise properties of the final combined images, the background pixel histograms of these images should show deviations from a Gaussian distribution in the form of high flux tails. No such deviations were ever observed in the histograms inspected at different background locations in the final images.

## 3.4. WFPC2/GSS Photometric Zeropoints

All total F814W fluxes  $F_{814}$  (galaxy, bulge or disk) will be converted in this paper to F814W magnitudes on the Vega system (denoted  $I_{814}$  or simply I hereafter) using the equation:

$$I_{814} = -2.5 \log_{10}(F_{814}/t_{814}) + C_{814},$$
 (1)

where  $C_{814} = 21.65$  (May 1997 WFPC2 SYNPHOT update).

Similarly, all total F606W fluxes  $F_{606}$  (galaxy, bulge or disk) were converted to F606W magnitudes on the Vega system (denoted  $V_{606}$  or simply V hereafter) using the equation:

$$V_{606} = -2.5 \log_{10}(F_{606}/t_{606}) + C_{606}, \tag{2}$$

where  $C_{606}=22.91$  (May 1997 WFPC2 SYNPHOT update). The total exposure time  $t_{814}$  was 4400 seconds in the F814W filter, and the total exposure time  $t_{606}$  was

<sup>10</sup> An image stack is defined here as a set of consecutive exposures taken at the same location on the sky and through the same filter.

2800 seconds in the F606W filter in all GSS fields except Field 7 for which  $t_{814}=25200$  seconds and  $t_{606}=24400$  seconds.

#### 4. SOURCE DETECTION, DEBLENDING AND EXTRACTION

To proceed with the fitting of galaxy images, GIM2D needs a catalog of sources for each image to be analyzed. For each source the catalog must include a x-y centroid position, an initial estimate of the local sky background level and the isophotal area of the object in pixels above the detection threshold. GIM2D also needs a segmentation or mask image in which pixels belonging to the same object are all assigned the same flag value and sky background pixels are flagged by zeroes. The source catalogs and segmentation images for the Groth Strip were created using the SExtractor ("Source Extractor") galaxy photometry package version 1.0a (Bertin & Arnouts 1996).

## 4.1. Detection Parameters

The SExtractor source detection was run on the CRREJ-combined  $I_{814}$  GSS images. The detection threshold was 1.5- $\sigma_{bkg}$ , and the required minimum object area above that threshold was 10 pixels. The convolution kernel was a  $3\times3$  Gaussian kernel with a FWHM of 1.5 pixels. These detection parameters do not have to be particularly fine-tuned to extract the faintest possible sources from the GSS images since the faintest magnitude at which reliable bulge+disk decompositions can be performed is well above the magnitude limits of the SExtractor source catalog. No star/galaxy separation was attempted. Every source was fitted with GIM2D. Unresolved sources such as stars could easily be identified as GIM2D output models with zero half-light radius.

#### 4.2. Deblending

As SExtractor performs source detection and photometry, it is able to deblend sources using flux multithresholding. This deblending technique works well in the presence of saddle points in the light profiles between objects. Each SExtractor pre-deblending "object" consists of all the pixels above the detection threshold that are spatially connected to one another. This group of pixels may or may not include several real objects. For each "object," the multi-thresholding algorithm goes through its connected pixels and rethresholds them at N levels (N = 32 in the current analysis) between the  $1.5\sigma_{bka}$ isophote and the peak pixel value in the "object" to build a two-dimensional flux tree of the "object." The algorithm then goes down the threshold levels, and it looks at each branch in the tree to see if the flux contained in that branch above the threshold level is a fraction  $f_{sep}$  or greater of the total flux in the "object." If a given branch meets this condition, it is then treated as a separate object, and the separation threshold for that object is set to the threshold at which the split occurred. The multi-thresholding algorithm assigns the pixels between two adjacent objects and below the separation threshold based on a probability calculated from bivariate Gaussian fits to the two objects. No assumption is made regarding the shape of the objects in this statistical deblending technique.

The fraction  $f_{sep}$  is set by the SExtractor input parameter DEBLEND\_MINCONT. A value of 0.00075 was used

for the SExtractor GSS source catalogs. This value is *subjective*, and it was found through visual inspection of several GSS fields to provide good object separation. Even though the value of DEBLEND\_MINCONT was determined subjectively, it provides an unequivocal definition of an object in the GSS catalogs presented in this paper. It was only determined once, and the same value of DEBLEND\_MINCONT was consistently used for all GSS fields as well as for all GSS simulations.

Figure 1 shows a typical section of the Groth Strip taken through the F814W filter (DEEP/GSS Field ID 8/WFC Chip 3), and Figure 2 shows the corresponding SExtractor segmentation image.

#### 4.3. Thumbnail Image Extraction

GIM2D disk+bulge decompositions are performed on thumbnail (or "postage stamp") images extracted around the objects detected by SExtractor rather than on the entire science image itself. Thumbnail images are preferable for two reasons: (1) Thumbnail images reduce the memory and I/O footprints of the program so it can be used in background mode on many computers without significantly impacting their other users. (2) Many CPUs can work on the same science image at the same time as they work on different thumbnail images. This is extremely useful since the same list of thumbnail images can be sent to all available CPUs on a network/cluster, and all CPUs will work down the same master list without interfering with one another. There is no limit on the number of CPUs that can be simultaneously harnessed for a given master list.

GIM2D will extract two or three thumbnail images for each object in the SExtractor catalog. The area of an object's thumbnail images is given by the isophotal area of the object. Here, all thumbnails were chosen to have an area 20 times larger than the 1.5- $\sigma_{bkq}$  isophotal area. The first thumbnail is extracted from the science image itself, and the local background calculated by SExtractor is subtracted from it so that it should have a background mean level close to zero. The second thumbnail is extracted from the SExtractor segmentation image. This segmentation thumbnail is modified so that bad pixels identified by the DQF frames (see section 3.2) will be excluded from the surface brightness fits. Some HST image datasets, most notably NICMOS datasets, include a "sigma" image giving the expected background + Poisson noise at each pixel. If such a sigma image is available, GIM2D will automatically extract the third thumbnail image from it.

## 5. SURFACE BRIGHTNESS FITS

## 5.1. Point-Spread-Functions

GIM2D accepts four kinds of Point-Spread-Functions (PSFs): a 2D gaussian PSF, a delta function PSF, a user-given PSF or a TinyTim PSF. GIM2D automatically normalizes the total flux in all input PSFs to 1.0 to ensure that this step has been performed. The 2D gaussian PSF is generated by GIM2D with the seeing FWHM specified in the GIM2D parameter file. If the delta function PSF option is selected, no PSF-convolution is performed on the galaxy image models. PSF effects should not be important for structures spanning a large number of resolution elements. Fits without PSF convolution require considerably

less computation time, a definite advantage for very large objects. The third kind of PSF is usually an image given by the user. For example, this image could be a bright star extracted directly from the image or could be created from a set of PSF stars using a stellar photometry program such as DAOPHOT (Stetson 1987). This option is particularly useful for ground-based studies in which sufficiently sampled PSF stars are easily found all over the science frames. TinyTim PSFs are generated by the Space Telescope Science Institute package TINY TIM (Krist 1993) version 4.4. TinyTim PSFs are available for all major imaging instruments onboard HST including WPFC2 and NICMOS. WFPC2 TinyTim PSFs were used for all (small and large) objects in the GSS analysis here.

The shape of the HST/WFPC2 PSF varies significantly as a function of position. Therefore, F814W and F606WPSFs were generated with TinyTim for each GSS object analyzed here. All GSS PSFs were oversampled by a factor of 5 and were 2".4 on a side. No telescope jitter was added. The pointing stability of HST in fine lock mode is typically better than 5 mas RMS, and any value under 7 mas is not noticeable (Krist 1993). WFPC2 charge-coupled devices (as any other CCDs) suffer from charge diffusion. Charge diffusion contributes a small amount of blurring to the images, and TinyTim does include a WFPC2 subpixel response function to take charge diffusion into account. However, it is very important to mention that Tiny-Tim does not automatically apply this subpixel response function to oversampled PSFs. GIM2D automatically convolves the oversampled PSF-convolved galaxy model with the subpixel response function kernel given in Krist (1993) after the model has been rebinned to the WFC detector resolution.

#### 5.2. Galaxy Image Model

The bulge+disk model used in GIM2D and other works is obviously a simple approximation. After all, many real galaxies will exhibit more than two structural components such as nuclear sources, bars, spiral arms and HII regions. Even in the presence of only a bulge and a disk, the ellipticity and/or the position angles of these components might be functions of galactocentric distance. However, each new structural component or new layer of complexity added to the model comes with additional parameters that stretch the amount of information that can be reasonably extracted from small, low signal-to-noise images of distant galaxies. The simple bulge+disk model is a trade-off between a reasonable number of fitting parameters and a meaningful decomposition of galaxy images. Despite its relative simplicity, careful analysis of the parameters of the bulge+disk model can yield useful information regarding those higher layers of complexity. For example, a very large deviation between the position angles of the bulge and of the disk is usually a strong indication of the presence of a bar, so barred galaxies can be easily identified without individually looking at all the galaxies in the sample. Histograms of  $\Delta \phi \equiv |\phi_b - \phi_d|$ are indeed a powerful way of finding barred galaxies. The shape of such histograms typically shows a well defined peak at  $\Delta \phi = 0$  with a tail of outliers that turn out to be the barred galaxies. The bulge+disk model is also a good way to study the morphology of quasar host galaxies. In the presence of a strong, unresolved, central source, the radius of one of the model components will shrink to zero to accommodate the source, and the other component will shape itself after the host galaxy. So, if quasar nuclei are found predominantly in elliptical galaxies, the radius of the disk component would be the one to converge to zero. Differences in the F814W and F606W centroid can also provide information on the irregularity of galaxy shape. All these examples illustrate the fact that the apparent simplicity of the bulge+disk model should not mask the richness of information provided by the inter-comparison of its full set of parameters.

Nonetheless, the bulge+disk model used here (and in other works) also has important limitations: it has a unique center for the whole galaxy, and the intrinsic (i. e., before PSF convolution) ellipticity and position angle of each component do not change as a function of radius. This is in contrast to techniques such as isophotal ellipse fitting in which it is customary to let ellipticity, position angle and centroid vary from one ellipse to the next. The limitations of the bulge+disk model can yield results that are unexpected (or unsuspected!) at first glance. Consider a purely elliptical galaxy with no disk component whatsoever but with varying ellipticity and position angle with radius. A bulge+disk fit to such an object may converge to a model with a significant disk component (B/T < 1). The additional degrees of freedom provided by the disk component are used by the model to compensate for the varying ellipticity and position angle. The position angle difference between the bulge and disk components will thus reflect the position angle difference between the inner and outer isophotes of the galaxy, and the inclination angle of the disk component will reflect the ellipticity of the outer isophotes. If mergers in high-density environments such as galaxy clusters induce such changes in ellipticity and position angle with galactocentric radius, then the same range of bulge fraction may not select the same galaxies in clusters and in the field. In addition to possible deviations from a pure deVaucouleurs law, this behavior of the bulge+disk model explains why, for example, brightest cluster galaxies can often have bulge fractions as low as 0.4 (Nelson et al. 2002). Finally, a single center for the model makes it impossible to detect differences in bulge and disk centroids should they manifest themselves in some stages of the evolution of galaxies. Unfortunately, the above limitations cannot be adequately dealt with by adding more fitting parameters since the basic bulge+ disk model already has enough parameters to make the search for the best-fit solution arduous.

It should be kept in mind that the conventional "bulge/disk" nomenclature does not say anything about the internal kinematics of the components. The presence of a "disk" component does not necessarily imply the presence of an actual disk since many dynamically hot systems also have simple exponential profiles of the form given by Equation 5 below (Lin & Faber 1983; Kormendy 1985). Likewise a "bulge" may represent a brightened center due to a starburst rather than a genuine dynamically hot spheroid. To avoid any confusion between photometric structures and internal dynamics entities, the names "photobulge" (for "photometric bulge") and "photodisk" (for "photometric disk") will be used hereafter to refer to the

 $r^{1/n}$  and exponential components of galaxy light profiles respectively.

The 2D galaxy model used by GIM2D has a maximum of twelve parameters: the total flux F in data units (DU), the bulge fraction  $B/T (\equiv 0 \text{ for pure photodisk systems})$ , the photobulge semi-major axis effective radius  $r_e$ , the photobulge ellipticity e ( $e \equiv 1 - b/a$ ,  $b \equiv$  semi-minor axis,  $a \equiv \text{semi-major axis}$ , the photobulge position angle of the major axis  $\phi_b$  on the image (clockwise, y-axis  $\equiv 0$ ), the photodisk semi-major axis exponential scale length  $r_d$ (also denoted h in the literature), the photodisk inclination i (face-on  $\equiv 0$ ), the photodisk position angle  $\phi_d$  on the image, the subpixel dx and dy offsets of the model center with respect to the thumbnail science image center, the background residual level db, and the Sérsic index n. Twelve parameters is a maximum since one or more parameters can be frozen to their initial values if necessary depending on the scientific goals being pursued. The position angles  $\phi_b$  and  $\phi_d$  were not forced to be equal for two reasons: (1) a large difference between these position angles is a signature of barred galaxies, and (2) some observed galaxies do have bona fide photobulges that are not quite aligned with the photodisk position angle.

Two types of radii are in use in the literature: geometric mean (also known as "circular" or "equivalent") radii and semi-major axis radii. The same name i. e., "effective" is used for both types of radii, and confusion arises when the type of radius used for a given sample is not clearly specified. As noted above, the photobulge effective radius in the GIM2D image model is calculated with respect to the semi-major axis of the photobulge component. Since the geometric mean (or "circular") photobulge effective radius  $r_{e,circ}$  is given by  $\sqrt{ab}$ , it is related to the semi-major axis radius  $r_{e,sma}$  by the simple relation  $r_{e,circ} = r_{e,sma}\sqrt{1-e}$ . Similarly, the GIM2D semi-major axis photodisk scale length  $r_{d,sma}$  is related to the circular photodisk scale length by  $r_{e,circ} = r_{e,sma} \sqrt{1 - e_{disk}}$ where  $e_{disk}$  is the ellipticity of the photodisk. Given the thinness of galaxy disks and the great distances of highredshift galaxies, the GIM2D photodisk model does not need to include a vertical scale height, The inclination angle of this infinitely thin photodisk is calculated from the measured photodisk ellipticity as  $i = \arccos(\sqrt{1 - e_{disk}})$ assuming that face-on photodisks are perfectly circular. This relation between photodisk ellipticity and inclination is different from the prescriptions used locally in Tully-Fisher work (e.g., Courteau 1997) which must account for the effect of disk scale height on the observed ellipticity of highly-inclined spiral galaxies.

The first component ("photobulge") of the 2D surface brightness model used by GIM2D to fit galaxy images is a Sérsic profile of the form:

$$\Sigma(r) = \sum_{e} exp\{-k[(r/r_e)^{1/n} - 1]\},\tag{3}$$

where  $\Sigma(r)$  is the surface brightness at radius r (Sérsic 1968). The parameter k is set equal to 1.9992n-0.3271 so that  $r_e$  remains the projected radius enclosing half of the light in this component (Capaccioli 1989). The classical de Vaucouleurs profile has the special value n=4, and this value was chosen for the current analysis. This choice was motivated by studies of bulge profiles in local galaxies. Locally, there is evidence that the bulges of late-type spiral galaxies may be better fitted by an n

= 1 profile, whereas bright ellipticals and the bulges of early-type spiral galaxies follow an n=4 profile (de Jong 1996; Courteau et al. 1996; Andredakis 1998). Local latetype galaxies with n=1 bulges have  $B/T \leq 0.1$  (de Jong 1996). Since such bulges contain only 10% of the total galaxy light, low signal-to-noise measurements of late-type high-redshift galaxies make it very difficult to determine the Sérsic index. On the other hand, n is more important for bulge-dominated galaxies, and n = 4 is the expected value based on local early-type galaxies. Knowing that bright ellipticals and the bulges of early-type spirals are well-fitted by a de Vaucouleurs profile, a n = 4 bulge profile was therefore adopted as the canonical bulge fitting model here for the sake of continuity across the full range of morphological types. The total flux in the Sérsic photobulge component is calculated by integrating Equation 3 from r = 0 to infinity to obtain:

$$F_{\text{photobulge}} = 2\pi n e^k k^{-2n} r_e^2 \Gamma(2n) \Sigma_e \tag{4}$$

where  $\Gamma$  is the gamma function. For n=4,  $F_{\rm photobulge}=7.214\pi r_e^2\Sigma_e$ . The bulge component was collapsed to a point (zero radius) source anytime its effective radius was less than 0.02 (0.2 WFC pixel) when the bulge+disk model fits were performed.

The second component ("photodisk") of the GIM2D model is a simple exponential profile of the form:

$$\Sigma(r) = \Sigma_0 exp(-r/r_d). \tag{5}$$

 $\Sigma_0$  is the face-on central surface brightness. The photodisk is assumed to be infinitely thin. The total flux in the photodisk is given by:

$$F_{\text{photodisk}} = 2\pi r_d^2 \Sigma_0. \tag{6}$$

The projected surface brightness distribution of the photodisk inclined at any angle i was calculated by integrating Equation 5 over the areas in the face-on photodisk plane seen by each projected pixel. The disk component was collapsed to a point (zero radius) source anytime its disk scale length was less than 0.002 (0.2 WFC pixel) when the bulge+disk model fits were performed. Equations 3 and 5 are given in their circularly symmetric form for simplicity, but the GIM2D model certainly does not assume circular symmetry since it includes photobulge ellipticity and photodisk inclination as fitting parameters.

The optical thickness of disk galaxies remains a hotly debated issue locally (Valentijn 1994; Giovanelli et al. 1994; Disney et al. 1992; Valentijn 1990), and this issue obviously has important consequences for the interpretation of local and high-redshift photodisk data. The photodisk optical thickness is not one of the fitting parameters, but photodisks can be fitted with surface brightness profiles of different optical thicknesses given by the parameter  $C_{abs}$  in the equation:

 $m_{\text{photodisk,obs}} = m_{\text{photodisk,face-on}} + 2.5 C_{abs} \log(a/b)$  (7)

where  $m_{\rm photodisk,obs}$  is the observed photodisk total magnitude and  $m_{\rm photodisk,face-on}$  is the face-on photodisk total magnitude. a/b is again the axial ratio of the photodisk component. Allowable values for  $C_{abs}$  are between 0 (optically thin photodisks) and 1 (optically thick photodisks).

All GSS photodisk models used in this analysis were totally optically thin  $(C_{abs} = 0)$ . No internal absorption was applied to photobulges.

A PSF-deconvolved semi-major axis half-light radius  $r_{hl}$  was also computed for each galaxy by integrating the sum of Equations 3 and 5 out to infinity with the best fitting structural parameters. This half-light radius may be in error for galaxies with large differences between their photobulge and photodisk position angles.

The WFPC2 detector undersampling was taken into account by generating the surface brightness model on an oversampled grid, convolving it with the appropriate oversampled PSF, shifting its center according to dx and dy and rebinning the result to the detector resolution for direct comparison with the observed galaxy image. Letting dx and dy be free parameters in the fits also helps compensate for possible errors in the initial determinations of the galaxy centroid by SExtractor.

## 5.3. Types of Fits

Before describing each type of fit, the question of what is being fitted should be discussed. Some studies (e.g., Schade et al. 1996) "symmetrized" galaxy images before fitting with a bulge+disk model. Symmetrization removes any asymmetric structures around a chosen image pivot point, i.e., the galaxy image centroid. Symmetrization makes sense since the fitting model is itself symmetric, and asymmetries can affect the final values for the best-fitting parameters (e.g., Marleau & Simard 1998 and Section 7.3) of this paper) when these asymmetries are very strong. Other studies (e.g., Ratnatunga et al. 1999) do not use image symmetrization. Although image symmetrization is an option in GIM2D, it was not used for the GSS structural analysis. To symmetrize or not to symmetrize is really a "philosophical" choice. The result of image symmetrization depends strongly on the choice of pivot point. An error in pinpointing the location of the true pivot point may result in an artificial change in the size of the object being fitted. The ambiguity on the true location of the galaxy centroid will increase with the strength of the asymmetric structure. So, as symmetrization would become more and more useful, the error introduced by a bad pivot point is also prone to become larger. Since symmetrization is not used here, possible effects of asymmetric structures on fitting parameters should be kept close to mind. For example, star-forming regions and spiral arms in the disk of galaxy can artificially increase the measured disk scale length and decrease the measured bulge fraction (Note that the problem can also affect symmetrized images if deviant structures were symmetric about the centroid of the galaxy). Fortunately, residual image indices (section 5.6) can be used to identify objects for which structural parameters may have been seriously compromised by asymmetric structures. An improved symmetrization procedure in which the total flux removed from the input image is minimized might solve the pivot point problem. The effects of asymmetries on the measured structural parameters from non-symmetrized fits are studied in detail in Section 7.3.

GIM2D offers three types of galaxy surface brightness fits: (1) two-bandpass, separate fits, (2) two-bandpass, simultaneous fits, and (3) single-bandpass, multiple image

fits. The first two types of fits were used for the GSS structural analysis, and the third one is particularly useful for dithered data such as used for HST/NICMOS. Science goals dictate the type of fits that should be used.

For the separate, two-bandpass fits, the GSS  $I_{814}$  and  $V_{606}$  thumbnail images were fitted independently, i. e., no fitting parameter was constrained to have the same value in both bandpasses. The only connection between the two bandpasses was the use of the  $I_{814}$  segmentation thumbnail image for both  $I_{814}$  and  $V_{606}$  fits. By comparing parameter values in both bandpasses, this type of fit can provide valuable information about color gradients in photobulges or in photodisks. These color gradients would yield very different photobulge effective radii or photodisk scale lengths in the two bandpasses. Also, the difference in the location of the  $I_{814}$  and  $V_{606}$  model centroids can be used as another image asymmetry estimate. For example, strong blue asymmetric structures possibly arising from star formation should perturb the centroid of the  $V_{606}$  model more than the  $I_{814}$  centroid. The main disadvantage of this type of fit is that it does not make maximum use of all the information available at a given signal-to-noise ratio. In the absence of color gradients, all the information should be used by fitting both bandpasses simultaneously as described below.

For the simultaneous, two-bandpass fits, the GSS  $I_{814}$  and  $V_{606}$  thumbnail images were fitted simultaneously with all but three fitting parameters forced to take on the same values in both bandpasses. The three fitting parameters allowed to be different were the total flux in the model (now  $F_I$  and  $F_V$ ), the bulge fraction (now  $(B/T)_I$  and  $(B/T)_V$ ) and the background residual level (now  $db_I$  and  $db_V$ ). This type of fit is, by its nature, blind to color gradients in the structural subcomponents, but, in the absence of such gradients, it should yield better photobulge and photodisk colors.

The third and last type of fit was not used for the DEEP/GSS analysis, but it deserves some discussion for its usefulness in fitting stacks of dithered images. Some WFPC2 and many NICMOS imaging programs consist of dithered exposures of the same region of the sky. The offsets between the images can be just a few pixels or they may be a significant fraction ( $\sim 1/3$ ) of the detector field of view. The offsets are often non-integer pixel shifts, and flux interpolation must be used in these cases to combine the images. Interpolation will affect the noise characteristics of the images and should be avoided. Significant flux errors can also be introduced by interpolating undersampled image data (e. g., WF and NICMOS/NIC3 cameras). The single-bandpass, multiple image fits use the same model to simultaneously fit multiple dithered images. GIM2D computes an image centroid for each image, and the image centroids are passed on to the model generating routine so that image models will be shifted accordingly. The main advantage here is the ability to avoid interpolating pixel flux.

All three types of GIM2D fits are performed on all pixels flagged as object or background in the SExtractor segmentation image. Object areas in the segmentation image are sharply delineated by the location of the isophote corresponding to the detection threshold (1.5- $\sigma_{bkg}$  here) since SExtractor considers all pixels below this threshold to be

background pixels. However, precious information on the outer parts of the galaxy profile may be contained in the pixels below that threshold, and fits should therefore not be restricted only to object pixels to avoid throwing that information away. Pixels belonging to objects in the neighborhood of the primary object being fitted are masked out of the fitting area using the SExtractor segmentation image. The flux from the primary object that would have been in those masked areas in the absence of neighbors is nonetheless properly included in the magnitude measurements given in this paper because magnitudes were obtained by integrating the best-fit models over all pixels.

## 5.4. Initial image moments and Fitting Parameter

Even though the SExtractor local background was subtracted from each science thumbnail image, GIM2D can compute a residual mean background level to correct for any error in SExtractor background estimates. GIM2D can also be instructed to compute its own estimate of  $\sigma_{bkq}$ . To compute background parameters, GIM2D uses all the pixels in the science thumbnail image flagged as background pixels (flag value of zero) in the SExtractor segmentation image. GIM2D further prunes this sample of background pixels by excluding any background pixel that is closer than five pixels from any (primary or neighboring) object pixels. This buffer zone ensures that the flux from all SExtracted objects in the image below all the 1.5- $\sigma_{bkq}$ isophotes does not significantly bias the mean background level upwards and artificially inflate  $\sigma_{bkq}$ . The GIM2D background parameters are tested in Section 7. For the GSS fits, background parameters were re-calculated with GIM2D before fitting, and the residual background levels db were then frozen to their recalculated values in the surface brightness fits.

SExtractor object centroid coordinates can be accepted as is, or GIM2D can determine its own intensity-weighted object centroid using a multi-threshold, minimum area procedure. This procedure first identifies which of three thresholds  $(10-\sigma_{bkg}, 5-\sigma_{bkg}, \text{ and } 3-\sigma_{bkg})$  has enough object pixels, as flagged by the SExtractor segmentation image, to meet a certain minimum area requirement. This minimum area was set to 8 for the GSS objects. GIM2D then computes intensity-weighted centroid coordinates at the highest level with enough pixels. If none of the three thresholds provides enough pixels to calculate the centroid, then GIM2D simply uses all object pixels to compute the centroid.

It is possible to place generous initial limits on certain structural parameters (total flux, initial photobulge and photodisk scale radii and position angles) based on simple image moments widely in use throughout the literature. For a given object, these moments are computed about the image centroid over the object pixels. These moments include:

$$M_{tot} = \sum_{i,j} I_{ij} \tag{8a}$$

$$M_{xx} = \frac{1}{M_{tot}} \sum_{i,i} x_{ij}^2 I_{ij} \tag{8b}$$

$$M_{yy} = \frac{1}{M_{tot}} \sum_{i,j} y_{ij}^2 I_{ij}$$
 (8c)

$$M_{xy} = \frac{1}{M_{tot}} \sum_{i,j} x_{ij} y_{ij} I_{ij}$$
 (8d)

$$M_{rr} = \frac{1}{M_{tot}} \sum_{i,j} (\sqrt{x_{ij}^2 + y_{ij}^2}) I_{ij}$$
 (8e)

where the sums are over the total number of pixels belonging to the object,  $x_{ij}$  and  $y_{ij}$  are pixel coordinates with respect to the object centroid, and  $I_{ij}$  is the background-subtracted pixel flux in the (i,j)th pixel. The initial total flux estimate for the image model is given by Equation 8a, and the maximum limit on this total flux is set to twice  $M_{tot}$ . The initial values for the photobulge effective radius and photodisk scale length are both set to the intensity-weighted average radius of Equation 8e, and the maximum limits placed on these two scale radii are set to twice the intensity-weighted average radius  $M_{rr}$ . The minimum limits on the two scale radii are set to zero to allow the model to fit unresolved sources if needed.

The object position angle is another parameter that can be set to an initial value given by the image moments above as:

$$\phi = \frac{1}{2} \arctan\left(\frac{2M_{xy}}{M_{yy} - M_{xx}}\right) \tag{9}$$

So, both  $\phi_b$  and  $\phi_d$  are initially set to  $\phi$ . No minimum/maximum limits are placed on the photobulge and photodisk position angles since Equation 9 is a circular function. In the case of a perfectly circular object  $(M_{xx} = M_{yy})$ , both  $\phi_b$  and  $\phi_d$  are set to zero. Both parameters are given generous initial Metropolis "temperatures" (see next section) of  $60^{\circ}$ .

#### 5.5. Metropolis Fitting Algorithm

The 12-dimensional parameter space can have a very complicated topology with local minima at low S/N ratios. It was therefore important to choose an algorithm which did not easily get fooled by these local minima. The Metropolis algorithm (Metropolis et al. 1953; Saha & Williams 1994) was designed to search for optimal parameter values in a complicated topology, and it is widely used in many fields of physics and computer science. Compared to gradient search methods, the Metropolis algorithm is not efficient, i. e., it is CPU intensive. On the other hand, gradient searches are "greedy." They will start from initial parameter values, dive in the first minimum they encounter and claim it is the global one.

The first step in the fitting process is the "initial condition filter" (ICF). The ICF coarsely samples the very large volume of structural parameter space  $V_0$  defined by broad limits from the initial image moments (Section 5.4) and user-specified parameter constraints to determine a promising sub-volume to be explored by the Metropolis algorithm. The uniform ICF sampling for the  $i^{th}$  structural parameter follows the equation:

$$\Delta x_i = x_{i,0} + (u - \frac{1}{2})T_i \tag{10}$$

where  $\Delta x_i$  is a trial step in parameter space,  $x_{i,0}$  is the  $i^{th}$  coordinate of the ICF sampling origin given by the

image moments and user constraints, u is a uniform deviate between 0 and 1, and  $T_i$  is the "Metropolis temperature" of the parameter. The Metropolis temperature of a parameter is given in the same units as that parameter. The ICF samples parameter space with  $N_{ICF}$  (set to 400 here) different galaxy image models and keeps track of which model yields the highest likelihood. The appropriate value of  $N_{ICF}$  depends on how well constrained the search volume is initially. After completion, the ICF sets the sampling origin to the parameters of that best ICF model. The volume  $V_0$  is reduced by a factor of  $N_{ICF}$  by cooling each Metropolis parameter temperature according to  $T_i'=T_i/(N_{ICF})^{1/n}$  with n=12 being the number of fitting parameters in the galaxy image model used here. The new sampling origin, the reduced search volume, and the cooler Metropolis parameter temperatures are then sent to the Metropolis algorithm to continue the search further.

The Metropolis algorithm in GIM2D starts from the sampling origin given by the ICF and computes the likelihood  $P(\overline{\mathbf{w}}|D,M)$  that the parameter set  $\overline{\mathbf{w}}$  is the true one given the data D and the model M. It then generates random perturbations  $\Delta \overline{\mathbf{x}}$  about that initial location with a given "temperature." When the search is "hot," large perturbations are tried. After each trial perturbation, the Metropolis algorithm computes the likelihood value  $P_1$  at the new location, and immediately accepts the trial perturbation if  $P_1$  is greater than the old value  $P_0$ . However, if  $P_1 < P_0$ , then the Metropolis algorithm will accept the trial perturbation only  $P_1/P_0$  of the time. Therefore, the Metropolis algorithm will sometimes accept trial perturbations which take it to regions of lower likelihood. This apparently strange behavior is very valuable: if the Metropolis algorithm finds a minimum, it will try to get out of it, but it will only have a finite probability (related to the depth of the minimum) of succeeding. The "temperature" is regulated according to the number of accepted iterations. If the Metropolis accepts too many trial perturbations, then the search is too "cold," and the temperature must be increased. Conversely, if the Metropolis rejects too many trial perturbations, then the search is too "hot," and the temperature must be decreased. The Metropolis temperature is regulated such that half of the trial perturbations are accepted. The temperature is checked every fiftieth iteration, and the terms of the covariance matrix s are adjusted according to whether the search is too hot or too cold. The more commonly known "simulated annealing" technique is a variant and a special case of the Metropolis algorithm in which the temperature is only allowed to decrease until a "ground-state" is reached.

The step matrix for the trial perturbations  $\Delta \overline{\mathbf{x}}$  is given by the simple equation  $\Delta \overline{\mathbf{x}} = \mathbf{Q} \cdot \overline{\mathbf{u}}$ , where the vector  $\overline{\mathbf{u}}$  consists of randomly generated numbers between -1 and 1. The matrix  $\mathbf{Q}$  thus controls the step distribution, and random steps with any desired covariance can be generated by solving the equation  $\mathbf{s} = \mathbf{Q} \cdot \mathbf{Q}^T$  through Choleski inversion. The matrix  $\mathbf{s}$  is the local covariance matrix of accepted iterations (Vanderbilt & Louie (1984)). In short, the Metropolis sampling of parameter space shapes itself to the local topology.

Convergence is achieved when the difference between two likelihood values separated by 100 iterations is less than  $3\sigma$  of the likelihood fluctuations. After convergence, the Metropolis algorithm Monte-Carlo samples the region where the likelihood is thus maximized and stores the accepted parameter sets as it goes along to build the distribution  $P(\overline{\mathbf{w}}|D,M)$ . Once the region has been sufficiently sampled  $(N_{sample}=300 \text{ here})$ , the Metropolis algorithm computes the median of  $P(\overline{\mathbf{w}}|D,M)$  for each model parameter as well as the 68% confidence limits. The output of the fitting process consists of a PSF-convolved model image O, a residual image R and a log file containing all Metropolis algorithm iterations, the final parameter values and their confidence intervals.

GIM2D creates two output images for each fitted object: an image of the PSF-convolved model and an image showing the residuals from the bulge+disk model subtraction. Figure 3 shows mosaics (science, GIM2D output models, and residual) of 35 GSS galaxies with  $I_{814} \leq 24$  chosen at random from the whole GSS sample. All three mosaics use the same greyscale levels. The  $I_{814}$  magnitude, bulge fraction and semi-major axis half-light radius are given on the original images.

## 5.6. Residual Image and Asymmetry Indices

GIM2D computes six image indices from the thumbnail residual image that can be used to globally characterize the structures left after the best galaxy image model has been subtracted.

The first indices,  $R_T$  and  $R_A$ , were first applied to distant galaxies by Schade et al. (1995). These indices are based on local studies of spiral arm patterns (Elmegreen, Elmegreen, & Montenegro 1992), and they provide an estimate of the overall smoothness of the galaxy image with respect to the fitting model. Following Schade et al. (1995),  $R_T$  and  $R_A$  are defined as:

$$R_{T} = (R_{T})_{raw} - (R_{T})_{bkg}$$

$$= \frac{\sum_{i,j} \frac{1}{2} |R_{ij} + R_{ij}^{180}|}{\sum_{i,j} I_{ij}} - \frac{\sum_{i,j} \frac{1}{2} |B_{ij} + B_{ij}^{180}|}{\sum_{i,j} I_{ij}}$$
(11a)
$$R_{A} = (R_{A})_{raw} - (R_{A})_{bkg}$$

$$= \frac{\sum_{i,j} \frac{1}{2} |R_{ij} - R_{ij}^{180}|}{\sum_{i,j} I_{ij}} - \frac{\sum_{i,j} \frac{1}{2} |B_{ij} - B_{ij}^{180}|}{\sum_{i,j} I_{ij}}$$
(11b)

where the  $R_{i,j}$ 's are pixel values in the residual image, and the  $R_{ij}^{180}$ 's are pixel values in the residual image rotated by  $180^{\circ}$ . Since these raw values  $(R_T)_{raw}$  and  $(R_A)_{raw}$  involve taking absolute values of pixel fluxes, they will yield a positive signal even in the sole presence of white noise. These raw values must therefore be background-corrected. The background corrections,  $(R_T)_{bkg}$  and  $(R_A)_{bkg}$ , are computed over pixels flagged as background pixels in the SExtractor segmentation image. The  $B_{i,j}$ 's are background pixel values in the residual image, and the  $B_{ij}^{180}$ 's are background pixel values in the residual image rotated by  $180^{\circ}$ . The background corrections are computed over a background pixel area equal to the pixel areas over which the raw indices were computed.  $B_{i,j}$ 's were randomly drawn from the full pool of all background pixels in the thumbnail

science image to decrease the vulnerability of background parameter determination to possible localized background image artifacts.

There is a fundamental difference between the  $R_T$  and  $R_A$  indices of Schade et al. (1995) and the ones implemented in GIM2D. Schade et al. calculated residual indices within a physical radius of 5 kpc irrespective of the physical size of the whole galaxy. On the other hand, GIM2D computes its  $R_T$  and  $R_A$  indices within ten circular apertures whose radii are multiples of the galaxy halflight radius  $r_{hl}$  ranging from 1  $r_{hl}$  to 10  $r_{hl}$ . The GIM2D  $R_T$  and  $R_A$  indices therefore sample the same fractional area for all galaxies. Schade et al. define normal galaxies as galaxies with  $R_T + R_A \leq 0.14$ . Im et al. (2001) were able to define a sample of high-redshift E/SO purely based on quantitative morphology with only two simple selection criteria  $((B/T)_I > 0.4 \text{ and } R_T + R_A \leq 0.08)$ , and McIntosh (2001) used  $R_T + R_A$  to study the S0 populations of a sample of local Abell clusters. Measuring  $R_T$  and  $R_A$ in different bandpasses could also show the wavelengthdependence of the strength of residual structures. If  $R_T$ and  $R_A$  have larger values in bluer bandpasses (e. g.,  $V_{606}$ versus  $I_{814}$ ), then this would suggest that asymmetries arise from star-forming regions. For example, there appears to be a correlation between the strength of residual structures and star formation rates measured from [OII] emission lines in galaxies in poor groups (Tran et al. 2001).

The next two image indices are from the automated classification proposed by Abraham et al. (1994, 1996). This classification relies on two parameters: one measuring the concentration of galaxy light (C) and the other one measuring image asymmetry (A). The so-called C-A system explicitly takes the ellipticity of galaxy images into account instead of simply using circular apertures. The image moments are used to define an equivalent elliptical distribution. For each object, the area  $A_{2\sigma}$  of the  $2-\sigma_{bkg}$  isophote is first computed. Then, following Abraham et al. (1994), the definitions of the concentration index C and normalized radius  $r_{ij}$  are:

$$C(\alpha) = \frac{\sum_{(i,j)\in E(r_{ij}\leq \alpha)} I_{ij}}{\sum_{(i,j)\in E(r_{ij}\leq 1)} I_{ij}}$$
(12a)

$$r_{ij} = M_{yy}x_{ij}^2 + M_{xx}y_{ij}^2 - 2M_{xy}x_{ij}y_{ij}$$
 (12b)

where  $E(r_{ij})$  is an elliptical aperture bounded by  $r_{ij}$ , i. e.,  $r_{ij}$  is constant on elliptical isophotes, and the image moments are normalized such  $E(1) = A_{2\sigma}$ . Abraham et al. adopted a value of  $\alpha = 0.3$ .  $C(\alpha)$  was computed for four values of  $\alpha$  (0.1, 0.2, 0.3, and 0.4) for the GSS galaxies. The A parameter measures image asymmetry in a similar way to  $R_A$ . However, A is computed directly on the science image whereas  $R_A$  is computed on the residual image from the bulge+disk fit. A is also computed over the area  $A_{2\sigma}$ , and again similarly to  $R_A$ , a background correction must be applied to raw A values to remove the extra positive signal from the background image noise. The C-A indices have been implemented in GIM2D exactly as prescribed by Abraham et al. (1996). Subsequent works (e.g., Conselice, Bershady, & Jangren 2000; Wu 1999) have since shown

that choosing an image pivot point which minimizes the measured asymmetry greatly improves the classification results, but these improvements have not been included in GIM2D yet.

In addition to the previous indices, two new indices,  $A_z$  and  $D_z$ , were defined to quantify residual asymmetric structures. The  $A_z$  index is calculated over the pixels belonging to the object or the background. Each pixel is compared to its symmetrical counterpart about the center of the object. If the flux in that pixel is  $n\sigma_{bkg}$  higher than the flux in its symmetrical counterpart, then the pixel is taken to be part of an asymmetrical component.  $A_z$  is the sum of the fluxes of all such pixels normalized by the total object flux. The  $A_z$  index is computed for n = 2, 3 and 5 within circular annuli with radii between  $1r_{hl}$  and  $10r_{hl}$ . A statistical background correction similar to the ones used for  $(R_T)$  and  $(R_A)$  was applied to the raw  $A_z$  values. The  $D_z$  index takes advantage of the isophotal shape of the object as measured by SExtractor.  $D_z$  is the sum of the fluxes of the object pixels (as given by the segmentation image) with symmetrical counterparts about the object center which do not belong to the object. This sum is normalized by the total object flux.  $D_z$  is computed outside of one half-light radius, and it is sensitive to asymmetries such as tidal arms.

### 6. STRUCTURAL CATALOGS

The images of GSS galaxies were fitted with both the separate and simultaneous fitting procedures, and extensive sets of GSS simulations were performed for both (Section 7). As a result, four structural parameter catalogs are presented in this paper: two science catalogs and two simulation catalogs. These catalogs are automatically generated from the GIM2D output log files by a set of scripts. These scripts calculate all the final parameter values including physical lengths and rest-frame quantities (Section 6.2 below) with full Monte-Carlo propagation of the parameter errors (Section 6.3 below). The Keck/LRIS spectroscopic redshifts used to compute physical radii in kiloparsecs and rest-frame magnitudes and colors for the whole galaxy, the photobulge and the photodisk are taken from Phillips et al. (2002). The observational, reduction and analysis procedures used to measure these redshifts are fully described in their paper.

## 6.1. Description

The contents of the science catalogs are listed in machine-readable Tables ?? (separate fits) and ?? (simultaneous fits). The separate fit science catalog contains 7450 objects, and each object has 330 columns of parameter information (including error bar columns). Simultaneous fits were performed only to objects with Keck/LRIS redshifts from the DEEP survey of the Groth Strip. The simultaneous catalog thus contains 648 objects with 279 columns of information for each one, including error bar columns. There are two error columns associated with each entry described in Tables ?? and ??: one for the lower 68% confidence bound and the other for the upper 68% bound. Most of the column descriptions in Tables ?? and ?? are self-explanatory, but some of them require further details:

DEEP/GSS IDs "gssid": The internal DEEP/GSS object IDs ("gssid") are given by the format FFC-XXYY where FF is the GSS field (Table 1, Column 1), C is the WFPC2 chip number, and XX and YY are the object coordinates on the chips in units of 10 pixels. These internal IDs are extended with letters ("a", "b", "c", etc.) when a group of objects are close enough together that they would all have the same primary ID. In addition to these internal DEEP/GSS objects ID's, the catalogs list the J2000.0 coordinates of each object.

Physical scale lengths: All angular scale lengths  $(r_{hl}, r_e,$  and  $r_d)$  were converted to physical lengths according to the equation:

$$R = r \frac{c}{1000H_0} \frac{1}{1+z} \int_0^z \frac{dz'}{\sqrt{\Omega_m (1+z')^3 + \Omega_\Lambda}}$$
 (13)

where z is the redshift, c is the speed of light, r is the measured angular scale length in radians, and R is the corresponding physical length in kiloparsecs (Hogg 1999). Equation 13 is only valid for flat  $(\Omega_k \equiv 1 - \Omega_m - \Omega_\Lambda = 0)$  cosmologies.

Position angles on sky: The GIM2D photobulge and photodisk position angles  $\phi_{b,image}$  and  $\phi_{d,image}$  measured on the images clockwise with respect to the positive y-axis were converted to real position angles  $\phi_{b,sky}$  and  $\phi_{d,sky}$  on the sky using the telescope position angles stored in the HST image headers.

AB Magnitudes: Even though Vega-based magnitudes are primarily used in this paper, Tables ?? and ?? also provide AB magnitudes. To go from Vega to AB magnitudes, one uses  $I_{814}(AB) = I_{814}(Vega) + 0.44$  and  $V_{606}(AB) = V_{606}(Vega) + 0.11$ .

Galaxy rest-frame B-band photobulge fraction: The restframe photobulge fraction is given by the simple equation:

$$(B/T)_{B,rest} = 10.0^{(M_{B,galaxy} - M_{B,bulge})/2.5}$$
 (14)

where  $M_{B,\mathrm{galaxy}}$  and  $M_{B,\mathrm{bulge}}$  are the rest-frame B-band magnitudes of the galaxy and photobulge respectively. Since different k-corrections apply to the photobulge and photodisk stellar populations, the observed bulge fraction of a galaxy will change with redshift. So, rest-frame photobulge fractions make more uniform photobulge fraction selections possible.

#### 6.2. Rest-Frame Quantities

Rest-frame quantities in the GIM2D/GSS structural catalogs were calculated using two very different sets of k-corrections. These two sets provide independent checks of the reliability of the resulting rest-frame quantities. Rest-frame quantities were calculated independently for the total galaxy, the photobulge and the photodisk.

The first set of k-corrections (referred to as Gronwall k-corrections throughout this paper) is based on the work of Gronwall & Koo (1995). The corrections are based on eleven theoretical galaxy spectral energy distributions from the 1995 Bruzual and Charlot models. The parameters of these theoretical SEDs are given in Gronwall & Koo (1995). Some of these SEDs include dust and starbursting populations. The rest-frame magnitudes and colors of any galaxy are obtained by interpolating the SEDs. The input quantities are galaxy redshift, Vega-based  $I_{814}$ 

magnitude and  $V_{606} - I_{814}$  color. The output consists of rest-frame BVRI absolute magnitudes, rest-frame (U-B) and (B-V) colors, and rest-frame B and K magnitudes.

The second set of k-corrections (referred to as Willmer-Gebhardt or WG k-corrections throughout this paper, Gebhardt et al. 2002) is based on actual galaxy spectra. These spectra are taken from the Database of UV-Optical spectra of Nearby Quiescent and Active Galaxies (Kinney et al. 1996; Schmitt et al. 1997). This database has recently been expanded to include 99 galaxies, 48 of which have full wavelength coverage from 1200 to 10000Å with a combination of International Ultraviolet Explorer (IUE) and ground-based spectra. Filter bandpasses are convolved with the galaxy spectra to produce rest-frame (U-B) colors and B-band k-corrections  $k_B$ . A polynomial is fitted to the observed  $(V_{606} - I_{814})$  colors and the rest-frame (U-B) SED colors in each redshift range. The best-fit polynomial reproducing the data over the redshift range 0.1 - 1.1 is given by:

$$(U - B)_{WG} = -0.8079 - 0.049752z - 1.6232z^{2} + 1.04067z^{3}$$

$$+1.5294z^{4} - 0.41190z^{5} - 0.56986z^{6} + (0.61591)$$

$$+1.07249z - 2.2925z^{2} + 1.3370z^{3})(V_{606} - I_{814})$$

$$+(0.280481 - 0.387205z + 0.043121z^{2})$$

$$(V_{606} - I_{814})^{2}$$

$$(V_{606} - I_{814})^{2}$$

$$(15)$$

Similarly, the B-band k-corrections are given by:

$$k_{BI} = 0.0496 + 0.46057z + 1.40430z^{2} - 0.19436z^{3}$$

$$-0.2232z^{4} - 0.36506z^{5} + 0.17594z^{6} + (2.0532)$$

$$-2.8326z + 1.05580z^{2} - 0.67625z^{3})(V_{606} - I_{814})$$

$$+ (0.10826 - 0.68097z + 0.61781z^{2})(V_{606} - I_{814})^{2},$$
(16

and the rest-frame *B*-band magnitude in the Willmer-Gebhardt system is given by:

$$M_{B,\text{WG}} = I_{814} - DM(\Omega_m, \Omega_\Lambda, \Omega_k) + k_{BI}$$
 (17)  
where  $DM(\Omega_m, \Omega_\Lambda, \Omega_k)$  is the distance modulus for the adopted cosmology. See Gebhardt et al. (2002) for more details.

#### 6.3. Error Estimates

All parameter error estimates in the GIM2D/GSS structural parameter catalogs are 68% confidence limits. Many of these error estimates are asymmetric since they were derived through full Monte-Carlo propagations of the parameter probability distributions  $P(\overline{\mathbf{w}}|D,M)$  computed by GIM2D through all the transformations required to calculate a given final parameter. This process takes into account all the Gaussian and non-Gaussian covariances among the parameters. To illustrate the process, consider the observed photobulge  $I_{814}$  magnitude of a galaxy. This quantity depends on both the total galaxy model flux and the observed F814W bulge fraction. So, the parameter probability distributions  $P(F_{814}|D,M)$  and P(B/T|D,M)were first Monte-Carlo sampled 500 times, and a photobulge magnitude was calculated each time using Equation 1. The resulting 500 photobulge magnitudes were

then sorted, and the lower and upper 68% confidence error estimates were derived from that sorted distribution. Going one step further, the  $V_{606}$  photobulge magnitude can be computed in exactly the same way as  $I_{814}$ , and the resulting 500  $V_{606}-I_{814}$  colors can then be transformed to photobulge rest-frame B-band magnitudes using Equations 16 and 17 so that one can in turn compute the 68% lower and upper error estimates on the photobulge absolute magnitude.

#### 7. SIMULATIONS

Three sets of GIM2D simulations were run to characterize the systematic biases and random errors in the GIM2D/GSS structural measurements. These simulations are a key element in the interpretation of the observations, and the simulation catalogs are presented in the same way as real catalogs to emphasize this point. Given any real science plot, it is straightforward to select sets of simulated galaxies with the same selection criteria as the observations to immediately evaluate the biases and errors present in the data shown on that plot. The first set of simulations applies to separate fits of  $I_{814}$  and  $V_{606}$  GSS galaxy images (Section 7.1). It contains 5995 simulations, comparable in size to the real science catalog. The second set includes 5195 GSS simultaneous  $V_{606}/I_{814}$  fit simulations, and these simulations cover the full range of observed GSS photobulge and photodisk  $V_{606} - I_{814}$  colors (Section 7.2). The two sets of simulations above only include smooth galaxy image simulations. The effects of asymmetric structures on the measured structural parameters were explored with a third set of simulations described in Section 7.3.

## 7.1. Separate Fits

For the GSS separate fit simulations, 5995 smooth galaxy image models were created with structural parameters uniformly generated at random in the following ranges:  $20.0 \le I_{814} \le 25.0$ ,  $0.0 \le B/T \le 1.0$ ,  $0 \le r_e \le 0.7$ ,  $0.0 \le e \le 0.7$ ,  $0 \le r_d \le 0.7$ , and  $0 \le i \le 85^{\circ}$ . The Sérsic photobulge index was held fixed at n=4 for all models. Both photobulge and photodisk position angles were fixed to 90° for all simulations, and the bulge and disk sizes were uniformly generated in the log of the size ranges above. The goal of these simulations is to characterize biases and errors and not to simulate what the real Universe would look like through the GIM2D observational "lens." The uniformity of the parameter distributions adopted here is therefore perfectly suitable to the task even though real galaxy parameters (e. g., bulge fraction) may not be so distributed. In the same spirit, no correlations were imposed between the input parameters despite the fact that some parameters (e. g.,  $r_e$  and  $r_d$ ) may be correlated in some types of galaxies (e.g., Courteau et al. 1996).

Each simulation was convolved with a F814W TinyTim PSF. This PSF had the same parameters as the TinyTim F814W PSFs used in the GSS analysis (Section 5.1). The same PSF was used in both creating and analyzing the simulations, so the results will not include any error in the structural parameters due to PSF mismatch. Poisson deviates were used to add photon noise due to galaxy flux into the simulations. The noisy images were then embedded in a  $20'' \times 20''$  section of one of the real F814W GSS images

to provide a real background for the simulations. In addition to sky photon noise and detector read-out noise, the real background noise includes brightness fluctuations of very faint galaxies below the detection threshold. The simulations were SExtracted with exactly the same SExtractor parameter files (Sections 4.1 and 4.2) as used for the GSS analysis, and GIM2D extracted science and segmentation thumbnails from the simulations following exactly the same steps as for the real galaxies (Section 4.3). Finally, the GIM2D output log files were processed through the same scripts to produce a catalog of final recovered structural parameters. The content of this catalog is listed in Table ??.

## 7.1.1. Systematic and Random Errors

For the sake of simplicity, the main tool adopted here to visualize errors is a set of two-dimensional maps giving systematic and random errors at each position. It should therefore be kept in mind that these maps can only offer a limited representation of the complex multidimensional error functions. As the large number of parameters in Tables ?? and ?? indicates, a full description of all systematic and random errors over all of bulge+disk multivariate structural space would considerably add to the length of this paper. Therefore, the error analysis presented in this section will focus on only three main galaxy structural parameters: total apparent magnitude, bulge fraction and half-light radius. Errors on any other set of parameters can be described in the same way, and the simulation catalog can be used to tailor error analyses to the needs of the specific science goals being pursued.

The error maps can be cast in terms of input or recovered coordinates, and the choice of coordinate system depends on how the error maps will be used. Input coordinates (i. e., the "true" coordinates) can be used to compute errors that are to be applied to theoretical galaxy structural catalogs in order to convert them to observed quantities (e.g., Simard et al. 2002. To illustrate this process, let  $\overline{w_T}$  be the position of a mock galaxy in theoretical structural space, and let  $r_{hl,T}$  be its theoretical half-light radius. If the simulation catalog shows that the recovered half-light radii of galaxies at  $\overline{w_T}$  are systematically in error by an amount  $\Delta r_1$ , then let  $r'_{hl,T} = r_{hl,T} + \Delta r_1$ . This new radius  $r'_{hl,T}$  is not yet the same as an observed radius as it does not include a random error. The random error on the half-light radius  $\sigma(r_{hl,T})$  at  $\overline{w_T}$  can also be calculated from the simulation catalog, and another radius correction  $\Delta r_2$  drawn at random from a Gaussian distribution of width  $\sigma(r_{hl,T})$  can be applied to  $r'_{hl,T}$  to produce the final "observed" theoretical half-light radius. The second set of coordinates, the recovered quantities, is the simulation equivalent of observed quantities, and error maps cast in those coordinates can be directly compared to the real data to see how important errors are in different regions of the observational space.

Figures 4, 5, and 6 show maps of errors on the galaxy total magnitude  $I_{814}$ , galaxy half-light radius  $r_{hl}$  and galaxy bulge fraction (B/T) respectively as a function of galaxy magnitude and galaxy half-light radius for the DEEP/GSS separate structural fits. The two top panels in each figure show the mean parameter error (left-hand panels, top number in cells) and the 1- $\sigma$  parameter random er-

ror (right-hand panels, top number in cells) as a function of input galaxy magnitude and size. Each cell also gives the number of simulations created for that cell (bottom number). The simulations are not evenly distributed over the galaxy magnitude-log size plane since the simulations were uniformly generated in  $\log r_e$  and in  $\log r_d$ . The lower left-hand panels show the mean parameter error as a function of recovered galaxy magnitude and size, and the lower right-hand panels of the three figures show the actual DEEP/GSS magnitude-size data. The unresolved objects (log  $r_{hl,obs} \leq -1.5$ ) are nicely separated from the galaxies in these panels.

Figure 4 shows that the systematic errors on  $I_{814}$  galaxy magnitudes start to become significant ( $\Delta I_{814} \simeq -0.2$ ) fainter than  $I_{814} = 23.5$ , and that, at a given magnitude, errors are larger for the largest galaxies in the simulations (log  $r_{hl,input} \geq -0.25$ ). The random magnitude errors are about 0.05 for  $I_{814} \leq 23.0$  and 0.13 for  $I_{814} > 23.0$ . The systematic errors cast in terms of input or recovered coordinates are essentially the same since the errors are not large enough compared to the cell sizes (0.5 mag and 0.5  $\log r_{hl}$ ) to shift simulations from cell to cell. If galaxies were pure bulges or pure disks, then according to equations 4 or 6, systematic magnitude and size errors should be anti-correlated, i. e., given an observed surface brightness profile and an underestimate, say, of the total flux (positive magnitude error), the profile modelling should try to compensate for that magnitude underestimate by introducing a negative error in the size. This anti-correlation should still hold for composite systems. A comparison of Figures 4 and 5 does show that magnitude and size errors are typically anti-correlated. Magnitude and size errors are important for fainter and larger galaxies since their relatively low surface brightness makes them more vulnerable to sky estimate errors.

The error maps for the galaxy bulge fraction (Figure 6) show that bulge fractions are underestimated by about 0.15 at magnitudes fainter  $I_{814} = 23.5$  with random errors around 0.25. However, Figure 6 is not really the best way to truly understand the behavior of the recovered bulge fractions. There are in fact two expected biases in the bulge fractions, and these biases arise from two ingredients of the DEEP/GSS bulge+disk analysis: (1) bulge fractions are constrained to stay between 0 and 1, and (2) bulge+disk models were fitted to all detected objects irrespective of the signal-to-noise ratio (S/N) of their images. The constraint on the bulge fraction forces the recovered bulge fractions of both very low  $(B/T \simeq 0)$  and very high  $(B/T \simeq 1)$  systems to scatter above zero and below one, and this bias will affect all galaxies irrespective of their S/N ratios. The second bias is inherent to bulge+disk model fits to objects with different S/N ratio. Previous studies have adopted a two-tier approach to this problem. Schade et al. (1995, 1996) first fit pure bulge or pure disks to their objects and then decide upon visual inspection of the residuals whether a bulge+disk model would be more appropriate. Ratnatunga et al. 1999 fit bulge+disk models to objects above a certain signal-to-noise, and objects below that threshold are fitted only with either a pure bulge or a pure disk model.

A different approach was taken here to deal with the bulge+disk S/N bias. Bulge+disk models were fitted to

all detected objects here for simplicity and for the sake of producing homogeneous structural catalogs. Bulge+disk models will converge to a pure bulge or a pure disk model only when the signal-to-noise ratio is high enough to definitely establish the presence of one and only one structural component. At low S/N ratios, the model will always be able to "slip" in both structural components. For example, the model could make use of a very large disk component to compensate for an underestimate of the sky level that may have been computed during the fit to a pure bulge system, and this would artificially decrease the recovered bulge fraction. Low signal-to-noise can also be responsible for hiding the outer wing of steep surface brightness profiles such as the  $r^{1/4}$  profile into the background noise and thus making them harder to identify. Figure 7 best shows the bulge fraction biases for the DEEP/GSS separate structural fits. Figure 7 is similar to previous error maps except that the errors are now computed over input bulge fraction and input galaxy magnitude instead of magnitude and size. As expected, the B/T systematic errors in Figure 7 show that (1) B/T is indeed overestimated in the first B/T bin, (2) B/T is underestimated in the last B/T bin, and (3) the magnitudes of the discrepancies increase with magnitude. The homogeneous approach to bulge+disk model fitting adopted here is valid as long as the results are used in conjunction with careful error characterization from the simulation catalogs.

#### 7.2. Simultaneous Fits

The GSS simultaneous fit simulations use the  $I_{814}$  simulations of Section 7.1 as a starting point. A companion  $V_{606}$  simulation was created for each  $I_{814}$  image with the same structural parameters except for total flux and bulge fraction. The  $V_{606}$  total flux and bulge fraction were calculated from the F814W total flux and bulge fraction and from randomly generated photobulge and photodisk  $(V_{606} - I_{814})$  colors. The photobulge and photodisk  $(V_{606}-I_{814})$  colors were uniformly and independently generated in the range 0.5-2.2. This range of colors spans the full range of observed colors out to a redshift of z=1.1 in the DEEP/GSS survey (Phillips et al. 2002), and it allows one to study the effects on fitting results of differences in photobulge and photodisk colors. For  $I_{814}$  pure photobulge systems  $((B/T)_I = 1.0)$ , the F606W bulge fraction and total flux are given by:

$$(B/T)_V = 1.0$$
 (18a)

$$(B/T)_V = 1.0$$
 (18a)  
 $F_{tot,V} = F_{tot,I} \frac{t_V}{t_I} 10^{(1.26 - (V - I)_{photobulge})/2.5}$  (18b)

where  $F_{tot,I}$  and  $F_{tot,V}$  are total F814W and F606Wgalaxy model fluxes in DU respectively,  $t_I$  and  $t_V$  are the F814W and F606W total exposure times (4400 seconds and 2800 seconds), and  $(B/T)_I$  and  $(B/T)_V$  are the F814W and F606W photobulge fractions. The zeropoint difference between  $V_{606}$  and  $I_{814}$  is 1.26.

For  $I_{814}$  pure photodisk systems ( $(B/T)_I = 0.0$ ), the F606W bulge fraction and total flux are given by:

$$(B/T)_V = 0.0$$
 (19a)

$$(B/T)_V = 0.0$$
 (19a)  
 $F_{tot,V} = F_{tot,I} \frac{t_V}{t_I} 10^{(1.26 - (V - I)_{photodisk})/2.5}$  (19b)

For  $I_{814}$  composite galaxy systems (0 <  $(B/T)_I$  < 1), the F606W bulge fraction and total flux are given by the equations:

$$(B/T)_{V} = \left(\frac{1 - (B/T)_{I}}{(B/T)_{I}} 10^{\Delta(V-I)/2.5} + 1.0\right)^{-1}$$
(20a)  
$$F_{tot,V} = F_{tot,I} \frac{(B/T)_{I}}{(B/T)_{V}} \frac{t_{V}}{t_{I}} 10^{(1.26 - (V-I)_{photobulge})/2.5}$$
(20b)

where  $\Delta(V-I)=(V-I)_{\rm photobulge}-(V-I)_{\rm photodisk}$ . After adding in Poisson noise, the  $V_{606}$  simulations were also embedded in the corresponding  $20''\times 20''$  section of one of the real F606W GSS images. This section of the sky was identical to the one used for the  $I_{814}$  simulations. As was done for the separate fit simulations, the simultaneous fit simulations were processed in exactly the same way as the real galaxies to produce a catalog whose content is listed in Table  $\ref{table}$ . Note that, as for the observations, the  $I_{814}$  segmentation thumbnail images were used for both bandpasses in the simultaneous fits.

#### 7.2.1. Systematic and Random Errors

Figures 8, 9, and 10 show maps of errors on the galaxy total magnitude  $I_{814}$ , galaxy half-light radius  $r_{hl}$  and galaxy bulge fraction (B/T) respectively as a function of galaxy magnitude and galaxy half-light radius for the DEEP/GSS simultaneous structural fits (see Figures 4, 5, and 6 for the corresponding separate fit results). The two top panels show the mean parameter error (left-hand panels, top number in cells) and the 1- $\sigma$  parameter random error (right-hand panels, top number in cells) as a function of input galaxy magnitude and size. Each cell also gives the number of simulations created for that cell (bottom number). Again, the simulations are not evenly distributed over the galaxy magnitude-log size plane since the simulations were uniformly generated in log  $r_e$  and in log  $r_d$ . The lower left-hand panels show the mean parameter error as a function of recovered galaxy magnitude and size. The lower right-hand panels of the three figures show the actual DEEP/GSS magnitude-size data. The number of data points is not nearly as large as in Figures 4, 5, and 6 since simultaneous bandpass structural fits were performed only on DEEP/GSS galaxies with secure Keck/LRIS redshifts. The errors from the simultaneous structural fits behave the same way as the errors from the separate fits, and simultaneous fit errors seem to be slightly smaller than those from the separate fits as one would expect from simultaneously using all the information content of both bandpasses. However, the improvement in the errors may not be as marked as expected since the simultaneous fit simulations included varying bulge fraction and colors as additional input parameters.

Bulge and disk colors were included in the simultaneous structural fit simulations with the goal of testing how well they are recovered in the fits. Figure 11 shows the structural component colors recovered by GIM2D from simultaneous structural fit simulations for galaxies with  $r_{hl,814} \geq 0.15$ , and  $r_{hl,606} \geq 0.15$ . The  $V_{606}$  limits for the galaxy, bulge, and disk magnitudes were set to 26.0. The

nine panels show recovered  $V_{606}-I_{814}$  colors versus input  $V_{606}-I_{814}$  colors for the galaxy as a whole (top panels), the bulge (middle panels) and the disk (bottom panels) in three different magnitude ranges. The colors are all well recovered by the fits. The mean and rms color difference in the three magnitude ranges are  $(0.002,\,0.020)$ ,  $(0.010,\,0.034)$ , and  $(0.063,\,0.087)$  for the galaxy as a whole,  $(-0.001,\,0.255)$ ,  $(0.022,\,0.120)$ , and  $(0.034,\,0.186)$  for the bulge and  $(0.008,\,0.047)$ ,  $(0.006,\,0.211)$ , and  $(0.030,\,0.304)$  for the disk. There are no significant systematic color errors, and the rms scatter increases with magnitude.

Although the recovered colors show no systematic offsets from the input colors, there are interesting outliers in some panels of Figure 11. In the leftmost middle panel, some recovered bulge colors are much too blue compared to their input colors. The three most discrepant bulges  $((V_{606} - I_{814})_{input} \ge 1.9$  and  $(V_{606} - I_{814})_{recovered} \le 1.3)$  are all very red bulges with very blue disks  $((V_{606} - I_{814})_{input,disk} \le 0.90)$ , and their effective radius differs from the scale length of their disk by a factor of five or more. In contrast, the central middle panel  $(21 \leq I_{814}(bulge) < 22.0)$  shows recovered bulge colors which are too red for their input colors. The two outlier bulges  $((V_{606} - I_{814})_{input} \leq 1.0)$  with red recovered colors  $((V_{606} - I_{814})_{recovered} \ge 1.5)$  are quite blue compared to their disks  $((V_{606} - I_{814})_{input,disk} \ge 2.1)$ . One of the bulges has an effective radius that differs by a factor of 10 from the disk scale length, but the other has an effective radius comparable to the disk scale length. The central bottom panel shows recovered disk colors that are too blue compared to their input values. The two rightmost bottom outliers are very red disks with bluer bulges  $((V_{606} - I_{814})_{input,bulge} \le 1.0)$ , and their effective radius is different from the disk scale length by a factor of 20-23!

The outliers in Figure 11 lead to an important question: Is there a combination of bulge fraction, bulge/disk size ratio  $r_e/r_d$ , and bulge/disk colors for which bulges can be mistaken for disks and vice versa? Figure 12 shows the systematic error (mean error) on bulge fraction as a function of input bulge fraction and input log bulge/disk size ratio  $(r_e/r_d)$  for both the separate structural fit (SPF) simulations and the simultaneous structural fit (SMF) simulations. There are no regions of that plane in which bulge fractions are systematically in error. This confirms the absence of systematic deviations in bulge and disk colors in Figure 11. However, there are places (especially for very small or very large bulge/disk size ratios) where the minimum or the maximum bulge difference is quite large, and these extrema can account for the kind of color outliers seen in Figure 11.

## 7.3. Effects of Asymmetric Structures On Fitting Parameters

Non-smooth local features in a galaxy 2D light profile can alter the best parameters derived with GIM2D depending on their brightnesses and positions in the galaxy. For example, a very bright feature at the center of the galaxy will cause the bulge component to be overestimated. The effects of clumps or asymmetric features on the extracted smooth 2D profile parameters were studied by adding an asymmetric light component, in the form of one or multiple "blobs or HII regions," i. e., unresolved

sources convolved with the PSF, to simulated smooth 2D profile images.

The input parameters for generating the asymmetric features are the number of HII regions  $n_{HII}$ , the total flux in the HII regions as a fraction  $f_{HII}$  of the total galaxy flux, and the HII regions' maximum galactocentric distance  $r_{HII}$  in units of galaxy half-light radius. The positions of the HII regions were randomly distributed within a circular aperture defined by  $r_{HII}$ . No overall ellipticity or radial exponential weight was given to the spatial distributions of the HII regions. A radially weighted elliptical HII region distribution could originate with HII regions linked with an inclined galaxy disk, but the "HII regions" here are meant to represent all unresolved asymmetric structures, and asymmetric structures may or may not necessarily be associated with the disk components of galaxies.

The total asymmetric flux was distributed among HII regions using a simple recipe (below) with no attempt to include, say, a realistic HII luminosity function. The simple recipe produced asymmetric structures that visually looked reasonable. According to this adopted recipe, the flux  $F_{\mathrm{HII},i}$  allocated to the  $i^{th}$  HII region was generated at random between 0 and

$$F_{\text{HII},i}^{max} = \frac{1}{n_{HII} - (i-1)} \left( f_{HII} F_{\text{total,galaxy}} - \sum_{j=0}^{i-1} F_{\text{HII},j} \right)$$
(21)

where  $1 \leq i \leq n_{HII}$ ,  $F_{\rm total,galaxy}$  is the total model galaxy flux,  $F_{\rm HII,i}^{max}$  is the maximum flux available to the  $i^{th}$  HII region,  $F_{\rm HII,j}$  is the flux that was actually allocated to the  $j^{th}$  HII region, and  $F_{\rm HII,j=0}=0$ . So, the bracket in Equation 21 contains the total unallocated HII flux that remains after i-1 regions have been created. For  $i=n_{HII}$ ,  $F_{\rm HII,i}$  is automatically set to the left-over HII flux.

Asymmetric features superposed on the smooth profile were generated randomly for  $n_{HII} = 5$  and  $r_{HII} = 1.5r_{hl}$ . Fifteen identical models were created for each simulated galaxy. The first five models had no HII regions, and they were used to establish a comparison baseline. The remaining ten models were divided into five discrete flux levels  $(f_{HII} = 0.05, 0.10, 0.15, 0.20, 0.25)$  with two models at each level in order to sample the same range of residual fluxes as seen in the real GSS galaxies. This set of simulations contains 170 different galaxy models for a total of 2550 simulations. The galaxy models were created with the following structural parameters:  $m_{F814W}(AB) = 24.0$ ,  $B/T=0.3,\ r_e=0.112,\ e=0.2,\ r_d=0.132,\ i=20^\circ,\ \phi_b=\phi_d=60^\circ,\ {\rm and}\ n=4.0.$  These asymmetric image galaxy simulations were analyzed exactly the same way as the real data, and the biases in the parameter values recovered by GIM2D were then examined at each  $f_{HII}$  level.

Figures 13 and 14 show the median systematic error on the recovered B/T,  $r_{hl}$ , and  $I_{814}$  parameters as function of  $f_{HII}$  in different six magnitude-size ranges. Both the recovered total magnitude  $I_{814}$  and half-light radius  $r_{hl}$  show no trends with increasing  $f_{HII}$ , and the magnitude

and size offsets in each magnitude-size range are in agreement with the systematic errors shown in Figures 4 and 5. The bulge fraction is also fairly robust against asymmetries. The median bulge fraction error is only about 0.1-0.2 for galaxies with  $f_{HII} = 0.20 - 0.25$ . However, increasing asymmetric flux leads to increasing scatter in the bulge fractions, and this scatter is skewed towards lower bulge fractions i. e., bulge fraction is always underestimated when asymmetries matter in a galaxy. The asymmetry parameter  $R_A + R_T$  (bottom half of Figure 14) recovers most of the asymmetric flux in big, bright galaxies. Equally bright but smaller galaxies have measured  $R_A + R_T$  slightly lower than big galaxies possibly due to the fact that the centroid of the bulge+disk models was allowed to vary by  $\pm$  1 pixel ( $\pm 0.15$ ) in the fits, and a shift in centroid would always be used by the fitting algorithm to reduce the overall amount of asymmetry "seen" by the smooth model. The scatter in the recovered values of  $R_A + R_T$  is higher for higher asymmetric fluxes due to model centroiding errors introduced by the asymmetries themselves.  $R_A + R_T$  increasingly underestimates the asymmetric flux at fainter and fainter magnitudes as individual asymmetry sources become too faint to be picked out of the noise.

#### 8. SURVEY SELECTION FUNCTIONS

Generalizing the formalism developed in Simard et al. (1999), the observed distribution of galaxies in structural parameter space as a function of redshift  $\Psi_O(\overline{\mathbf{W}},z)$  is the result of any inherent changes in the resident<sup>11</sup> galaxy distribution  $\Psi_U(\overline{\mathbf{W}},z)$  in that space and of observational selection effects. Selection effects are likely to be significant given the wide range of structural parameters observed locally (Bender, Burstein & Faber 1992; Burstein et al. 1997). It is therefore important to carefully characterize selection effects to disentangle them from real changes in  $\Psi_U(\overline{\mathbf{W}},z)$ . The path from  $\Psi_U(\overline{\mathbf{W}},z)$  to  $\Psi_O(\overline{\mathbf{W}},z)$  is given by:

$$\Psi_O(\overline{\mathbf{W}},z) = S_{PS}(\overline{\mathbf{W}},z)S_{UP}(\overline{\mathbf{W}},z)\Psi_U(\overline{\mathbf{W}},z),$$
 (22) where  $\overline{\mathbf{W}}$  is the full set of intrinsic structural parameters (note the use of lower and upper cases to distinguish between apparent and intrinsic structural parameter sets here). The subscript  $UP$  stands for "Universe to Photometric sample," and the subscript  $PS$  stands for "Photometric sample to Spectroscopic sample." The resident galaxy distribution  $\Psi_U(\overline{\mathbf{W}},z)$  is not known a priori. Once the two selection functions in Equation 22 have been characterized, their product (denoted  $S_{US}$  hereafter) shows the volume of the structural parameter space where real galaxies would have been observed if they existed in that region at high redshift. The spectroscopic selection function  $S_{PS}(\overline{\mathbf{W}},z)$  is derived in Phillips et al. (2002), so the remainder of this section will focus on  $S_{UP}(\overline{\mathbf{W}},z)$ .

The selection function  $S_{UP}(\overline{\mathbf{W}}, z)$  contains the information needed to go from any sample of galaxies on the sky to the photometric catalog produced with SExtractor and reflects the adopted SExtractor detection parameters (detection threshold in sigmas, minimum detection area, etc.).

<sup>&</sup>lt;sup>11</sup> It is very important to note the use of the term "resident" here and throughout the rest of the paper to refer to the intrinsic galaxy population at a given redshift z. In the absence of real evolution in the galaxy population with redshift, all resident populations would be the same as the local population of galaxies.

The detection thresholding method used by SExtractor depends critically on galaxy apparent surface brightness. The probability that a given object will be detected depends on total flux F, bulge fraction B/T, photobulge effective radius  $r_e$ , photobulge ellipticity e, photodisk scale length  $r_d$ , and photodisk inclination i. For example, objects with larger B/T will be easier to detect because they are more concentrated, and large objects will be harder to detect than smaller ones at a fixed total flux. The selection function does not depend on the photobulge and photodisk position angles. However, note that the selection function will also depend on disk internal extinction (if any), but this dependence is neglected here since GSS galaxies were analyzed with optically thin disks ( $C_{abs} = 0$ , recall Equation 7 in Section 5.2). In practice,  $S_{UP}(\overline{\mathbf{W}}, z)$ is derived from the selection function  $S_{UP}(\overline{\mathbf{w}})$  determined as a function of the observed structural parameters. The transformation  $S_{UP}(\overline{\mathbf{w}}) \to S_{UP}(\overline{\mathbf{w}}, z)$  can be made in each redshift bin using k-corrections calculated with the median observed galaxy  $V_{606} - I_{814}$  color of the  $B/T \leq 0.2$  galaxies at that redshift and the cosmological scale relations for the assumed cosmology.

 $S_{UP}(\overline{\mathbf{w}})$  was constructed by generating 60,000 galaxy models with structural parameter values uniformly covering the ranges:  $20.0 \le I_{814} \le 25.0$ ,  $0.0 \le B/T \le 1.0$ ,  $0.00 \le r_d \le 10.00$ ,  $0 \le \sin i \le 0.9962$ . It is better here to uniformly generate disk inclinations in  $\sin i$  rather than in i since randomly oriented, optically thin disks in space are expected to have a uniform  $\sin i$  distribution. Each model galaxy was added, one at a time, to an empty  $20'' \times 20''$  section of a F814W HST/GSS image (same image section as used in Section 7.1). "Empty" here means that no objects were detected by SExtractor in that sky section with the same detection parameters used to construct the object catalog. Using an empty section of the GSS ensured that  $S_{UP}(\overline{\mathbf{w}})$  was constructed with the real background noise that was seen by the detection algorithm. The background noise included read-out, sky and the brightness fluctuations of very faint galaxies below the detection threshold. This last contribution to the background noise is particularly hard to model theoretically, and the current approach bypassed this problem. SExtractor was run on each simulation with the same parameters that were used to build the SExtractor catalog. The function  $S_{UP}(\overline{\mathbf{w}})$  was taken to be the fraction of galaxies successfully detected and measured by SExtractor at each location  $\overline{\mathbf{w}}$  in structural parameter space.

Figure 15 shows one-dimensional projections of  $S_{UP}(\overline{\mathbf{w}})$  onto each of the six structural parameters  $(F, B/T, r_e, e, r_d, \text{ and } i)$ . Different symbols show groups of galaxies with different bulge fractions. Clearly, some parameters are more important for the selection function than others, and bulge parameters are obviously more important for bulge-dominated galaxies and the same holds true for disk parameters. The selection function depends strongly on total apparent magnitude independent of bulge fraction, and bulge-dominated galaxies are more likely to be detected at all magnitudes than disk galaxies. The selection function for bulge-dominated galaxies decreases with increasing bulge effective radius out to  $r_e = 2$ " and remains relatively flat beyond that radius. There is a very weak dependence of  $S_{UP}(e)$  on bulge ellipticity. The se-

lection function for  $B/T \geq 0.2$  galaxies is nearly independent of disk scale length whereas the selection function for B/T < 0.2 galaxies decreases out to  $r_d = 2.2$ " and remains flat after that. There is virtually no dependence of  $S_{UP}$  on the disk inclination angle, and this is somewhat surprising given that more inclined, optically thin disks should be easier to detect. This apparent puzzle was resolved by generating a set of 60,000 pure disk galaxy models and re-computing  $S_{UP}$  with this new set. There was a clear dependence of  $S_{UP}$  on disk inclination for this puredisk galaxy set. The detectability of disks went from 0.55 at  $i \sim 0^{\circ}$  to 0.75 at  $i \sim 80^{\circ}$ . Given that the disk sample in the selection function shown in Figure 15 includes galaxies with bulge fractions between 0.0 and 0.2, it appears that even a small (luminosity-wise) de Vaucouleurs bulge can boost the detectability of a galaxy enough to mask out the disk inclination dependence of the selection function.

#### 9. COMPARISON WITH THE MEDIUM DEEP SURVEY

The Medium Deep Survey (MDS, Ratnatunga et al. 1999 and references therein) is the largest database of HST galaxy structural parameters in existence with 200,000 objects as of October 1998. The images analyzed by the MDS team consist of MDS WFPC2 pure parallel observations as well as of HST archival observations of randomly selected WFPC2 fields such as the Groth Strip and the Hubble Deep Field among others. The MDS team fitted the profiles of Groth Strip galaxies separately in  $V_{606}$  and  $I_{814}$  using a completely different analysis pipeline, a completely different likelihood maximization algorithm and a different bulge+disk model. The parameters of the MDS bulge+disk galaxy model are sky background, x-y centroid, orientation (bulge and disk are assumed to have the same position angle), bulge and disk axis ratios, bulge fraction B/T and the ratio of the bulge/disk half-light radii. The large sizes (thousands of objects each) of the MDS and DEEP/GIM2D Groth Strip structural catalogs make them ideally suited to run a check of one against the other. This is the first time that MDS results are compared against an independent work on such a scale.

The MDS Maximum-Likelihood Estimate (MLE) structural catalogs of the Groth Strip galaxies were extracted directly from the on-line MDS CD-ROMs, and the MDS catalogs were matched to the DEEP/GIM2D separate structural fit catalog using a matching radius of 0."8 and a maximum  $I_{814}$  magnitude difference of 1. The match yielded 7138 positive cross-identifications. The results of the match are shown in Figure 16. The top left-hand panel shows the GIM2D galaxy model  $I_{814}$  total magnitudes against the MDS galaxy model  $I_{814}$  total magnitudes. The long-dashed line is a one-to-one line, the filled circles are galaxies with  $|I_{814,GIM2D} - I_{814,MDS}| \le 0.2$  mag, and the open circles are galaxies with magnitude differences larger than 0.2 mag. The envelope of the data point distribution is clearly asymmetric with respect with the one-to-one line in its upper section i. e., GIM2D magnitudes for some objects are too faint with respect to MDS magnitudes. The asymmetry in the upper envelope is due to the fact that it is made up of two distributions. One distribution comes from real photometric errors, and the distribution of its points as a function of distance from the one-to-one line is symmetric with respect to the lower envelope. The second distribution inside the upper envelope contains the most discrepant objects, and it is due to the fact that objects are more finely split in the DEEP/GIM2D structural catalog than in the MDS catalog. Thus some single objects in the MDS catalog are two or more distinct objects in the DEEP/GIM2D catalog, and their DEEP/GIM2D magnitudes are therefore fainter.

The top right-hand panel of Figure 16 shows the GIM2D galaxy log half-light radii in arcseconds against the MDS radii for galaxies with  $I_{814} \leq 22$ . The long-dashed line is again the one-to-one line. The half-light radii are in excellent agreement with no systematic differences. The mean log radius difference (GIM2D-MDS) and rms scatter are (0.002, 0.049) for objects with  $\Delta I_{814} \leq 0.2$  mag (filled circles) and (-0.071, 0.168) for objects with  $\Delta I_{814} > 0.2$  mag (open circles). The rms scatter for the open circles is higher as one would expect from using different object splitting.

The GIM2D  $I_{814}$  bulge fractions are compared against MDS  $I_{814}$  bulge fractions for galaxies with  $I_{814} \leq 22$  in the last panel of Figure 16. The two vertical distributions at  $(B/T)_{MDS} = 0.0$  (pure disk systems) and at  $(B/T)_{MDS} = 1.0$  come from the MDS pipeline where objects below a certain S/N threshold and/or size are only fitted by a pure bulge or a pure disk model and not by the full bulge+disk model. Setting these points aside for now, the mean B/T difference (GIM2D-MDS) and rms scatter for intermediate B/T galaxies are (-0.021, 0.105) for the filled circles and (-0.046, 0.235) for the open circles. The slight systematic offset and the increased rms scatter for the open circles is not surprising since objects that were split differently are likely to be classified differently. The discrepancies between the MDS and GIM2D bulge fractions at  $(B/T)_{MDS} = 0$  and  $(B/T)_{MDS} = 1$  are best studied by looking at the two extremes where  $(B/T)_{GIM2D} \geq 0.5$  at  $(B/T)_{MDS} = 0$  and  $(B/T)_{GIM2D} \le 0.5$  at  $(B/T)_{MDS} =$ 1. In the first case, the objects are unresolved in both MDS and GIM2D catalogs. In the second case, there are different reasons behind the bulge fraction discrepancies. Nineteen objects have  $(B/T)_{GIM2D} \leq 0.5$  at  $(B/T)_{MDS} = 1$ , and each was visually inspected. Out of these 19 objects, 6 objects are irregular/peculiar galaxies or close pairs not separated in the MDS catalog, 2 are stars, 5 are single objects with  $(B/T)_{MDS,I814} = 1$  and  $(B/T)_{MDS,V606} \le 0.5$ , 3 are equally well fit by the MDS and GIM2D models, 2 are single objects with knots in their MDS  $I_{814}$  residual images, and 1 is a bad object match. Even though these discrepant objects are very interesting, they represent a very small fraction of both catalogs, and the MDS and GIM2D results are generally in good agreement.

#### 10. SUMMARY

The structural parameters of galaxies in the Groth Survey Strip were measured from archival HST images as part of a combined HST and Keck/LRIS survey of the Strip by the DEEP team. GSS galaxy surface brightness distributions were fitted with a 2D, PSF-convolved bulge+disk model using an implementation of the Metropolis algorithm to optimize model parameters. A total of 7450 galaxies were fitted separately in  $I_{814}$  and  $V_{606}$ . 648 galaxies with secure Keck/LRIS redshifts were also fitted simultaneously in both bandpasses. The structural catalogs in

clude image asymmetry parameters and rest-frame magnitudes and colors for bulge and disk components computed using two different sets of k-corrections.

This paper also provides full structural catalogs of two extensive sets of close to 6000 simulations to allow detailed characterizations of the systematic and random errors in separate and simultaneous structural fits at any location in structural parameter space. Error maps for galaxy magnitudes, half-light radii and bulge fractions are presented as examples. The simultaneous structural fit simulations include varying bulge and disk colors and show that bulge and disk colors can be reliably measured down to  $I_{814}(bulge)=23.5$  and  $I_{814}(disk)=23.5$ . Similar formats are used for the real and the simulation catalogs so that interested users can study biases associated with different selection criteria to see which criteria will make the best use of the real data for the specific science goals being pursued.

The effects of unresolved, "HII-region"-like asymmetric structures on fitting parameters were studied with a third set of 2550 simulations. Recovered total magnitudes, half-light radii and bulge fraction were, on average, robust against the presence of strong asymmetries with little or no systematic bias. However, the scatter in the recovered parameters increased with increasing asymmetric flux, and this increased scatter was skewed towards lower bulge fractions. Bulge fractions are always underestimated when the presence of strong asymmetries matters. The asymmetry parameter  $R_A + R_T$  was found to be a good estimate of the total asymmetric flux present in large, bright galaxies.

The photometric selection function of the survey was mapped over a wide range of magnitudes, bulge fractions, and bulge/disk sizes to delineate the volume of structural space favored by the source detection algorithm. The key quantity is surface brightness. At a given magnitude, larger galaxies are harder to detect, and disks are harder to detect than bulges since disk profiles are less compact. There is little or no dependence of the selection function on bulge ellipticity and disk inclination. The selection function, coupled with biases and errors from the simulations, gives a complete reproduction of the observational limits.

The structural parameters presented here were compared with the results from the Medium Deep Survey database. This is the first large scale comparison of MDS results against an independent source. The MDS and DEEP/GIM2D catalogs yields 7138 positive cross-identifications, and measurements of total magnitude, half-light radius and bulge fraction are all in good agreement with no systematic differences. Bulge fraction classifications are in disagreement for a small fraction of the galaxies.

The combination of the three essential ingredients of quantitative galaxy morphology (very large sets of structural measurements, detailed characterization of biases and errors, and mapping of the multidimensional photometric selection function) found in this paper is ideal to pursue direct comparisons between observations and the latest models of galaxy formation and evolution.

The development of GIM2D greatly benefited from the experiences of a core user group which includes Kim-Vy Tran, Brad Holden, Francine Marleau, Katherine Wu,

Sasha Hinkley, and Daniel McIntosh. L.S. is indebted to them for their help. Special thanks to Katherine Wu and Roelof de Jong for their very thorough readings of the manusript. L. S. acknowledges many insightful discussions with P. D. Simard that significantly improved this paper. L. S. also gratefully acknowledges partial financial support from the Natural Sciences and Engineering Research Council of Canada through the award of a Postdoctoral Fellowship. This work was supported by NSF grants AST95-29098 and 00-71198 and NASA/HST grants AR-07532.01, AR-06402.01 and AR-05801.01.

#### REFERENCES

Abraham, R. G., Valdes, F., Yee, H. K. C., & van den Bergh, S. 1994, ApJ, 432, 75
Abraham, R. G., Tanvir, N. R., Santiago, B. X., Ellis, R. S., Glazebrook, K., & van den Bergh, S. 1996, MNRAS, 279, 47
Andredakis, Y. C. 1998, MNRAS, 295, 725
Balogh, M. L., Smail, I., Bower, R. G., Ziegler, B. L, Smith, G. P., Davies, R. L., Gaztelu, A., Kneib, J.-P., & Ebeling, H. 2002, ApJ, 566, 123 566, 123

Bender, R., Burstein, D., & Faber, S.M. 1992, ApJ, 399, 462 Bendinelli, O. 1991, ApJ, 366, 599 Bertin, E. & Arnouts, S. 1996, A&AS, 117, 393

Burstein, D., Bender, R., Faber, S. M., & Nolthenius, R. 1997, AJ, 114, 1365

Capaccioli, M. 1989, in Corwin H.G., Bottinelli L., eds, The World

of Galaxies, Springer-Verlag, Berlin, p.208 Conselice, C. J., Bershady, M. A., & Jangren, A. 2000, ApJ, 529,

Courteau, S., de Jong, R. S., & Broeils, A. H. 1996, ApJ, 457, 73 Courteau, S. 1997, AJ, 114, 2402

de Jong, R. S. 1996, A&A, 118, 557

de Vaucouleurs, G. 1948, Ann. Astrophys., 11, 247 de Vaucouleurs, G. 1959. In *Handbuch der Physik*, vol. 53, Astrophysics IV: Stellar Systems, S. Flügge (ed.).

(Berlin:Springer-Verlag), p. 275 Disney, M., Burstein, D., Haynes, M. P., & Faber, S. M. 1992, Nature, 356, 114

Elmegreen, B. G., Elmegreen, D. M., & Montenegro, L. 1992, ApJS,

Fasano, G., Cristiani, S., Arnouts, S., & Filippi, M. 1998, AJ, 115, 1400

Gebhardt et al. 2002, ApJ, submitted.

Giovanelli, R., Haynes, M. P., Salzer, J. J., Wegner, G., da Costa, L. N., & Freudling, W. 1994, AJ, 107, 2036 Gronwall, C. & Koo, D. C. 1995, ApJ, 440

Groth, E. J., Kristian, J. A., Lynds, R., O'Neil, E. J., Jr., Balsano, R., & Rhodes, J. 1994, BAAS, 185, #53.09 Guzmán, R., Jangren, A., Koo, D. C., Bershady, M. A., & Simard,

L. 1998, ApJ, 495, 13

Hogg, D. W. 1999, astro-ph/9905116

Hubble, E. P. 1936, The Realm of the Nebulae. (New Haven: Yale University Press)

University Press).
Im et al. 2001, ApJ, in press.
Kinney, A. L., Calzetti, D., Bohlin, R., McQuade, K.,
Storchi-Bergmann, T., & Schmitt, H. R. 1996, ApJ, 467, 38
Koo, D. C. 1998, in Proceedings of IAU 23 Joint Discussion

11: "Redshift Surveys in the 21st Century," ed. A. P. Fairall

(Dordrecht:Kluwer) Koo et al. 2002, ApJ, in preparation. Kormendy, J. 1985, ApJ, 295, 73

Krist, J. 1993, in Astronomical Data Analysis Software and Systems II, 52, eds. Hanisch, R. J., Brissenden, R. J. V., and Barnes, J.

(A.S.P. Conference Series), p. 536 Lin, D. N. C. & Faber, S. M. 1983, ApJ, 266, 17 Maller, A. H., Simard, L., Guhathakurta, P., Hjorth, J., Jaunsen, A. O., Flores, R. A., & Primack, J. R. 2000, ApJ, 533, 194 Marleau, F. R., & Simard, L. 1998, ApJ, 505, 585. McIntosh, D. 2001, Ph. D Thesis, University of Arizona

Metropolis, N., Rosenbluth, A., Rosenbluth, M., Teller, A., & Teller, E. 1953, Journal of Chemical Physics, 21, 1087

Morgan, W. W. 1970. In *Spiral Structure of Our Galaxy*. Becker, W. and Contopoulos, G. (eds.). (Dordrecht: Reidel).

Naim, A., Lahav, O., Buta, R. J., Corwin, H. G., Jr., de Vaucouleurs, G., Dressler, A., Huchra, J. P., van den Bergh, S., Raychaudhury, S., Sodre, L., Jr., & Storrie-Lombardi, M. C. 1995, MNRAS, 274, 1107

Naim, A., Ratnatunga, K. H., & Griffiths, R. E. 1997, Ap.IS, 111

Naim, A., Ratnatunga, K. U., & Griffiths, R. E. 1997, ApJS, 111, 357

Nelson, A. E., Simard, L., Zaritsky, D., Dalcanton, J. J., & Gonzalez, A. H. 2002, ApJ, 567, 144 Odewahn, S. C. 1995, PASP, 107, 770 Odewahn, S. C., Windhorst, R. A., Driver, S. P., & Keel, W. C.

1996, ApJ, 472, L13

Phillips et al. 2002, ApJ, in preparation.

Pirenne, B., Micol, A., Durand, D., & Gaudet, S. 1988, in

Astronomical Data Analysis Software and Systems VII, A.S.P.

Conference Series, Vol. 145, 1998, R. Albrecht, R.N. Hook and H.A. Bushouse, eds.,p.341

Press, W. H., Teukolsky, S. A., Vetterling, W. T., & Flannery, B. P. 1992, Numerical Recipes in C: The Art of Scientific Computing,

Second Edition, Cambridge University Press Ratnatunga, K. U., Griffiths, R. E., & Ostrander, E. J. 1999, AJ,

118, 86 Rhodes, J, Refregier, A., & Groth, E. J. 2000, ApJ, 536, 79

Saha, P., & Williams, T.B. 1994, AJ, 107, 1295

Sérsic, J.L. 1968, Atlas de Galaxias Australes (Cordoba:

Observatorio Astronomica)

Schade, D., Lilly, S. J., Crampton, D., Hammer, F., Le Fevre, O., & Tresse, L. 1995, ApJ, 451, 1

Schade, D., Lilly, S. J., Le Fèvre, O., Hammer, F., & Crampton, D. 1996, ApJ, 464, 79 Schmitt, H. R., Kinney, A. L., Calzetti, D., & Storchi-Bergmann,

T. 1997, AJ, 114, 592 Simard, L. 1998 in Astronomical Data Analysis Software Systems

VII, 145, eds. Albrecht, R., Hook, R. N. and Bushouse, H. A. (A.S.P. Conference Series), p. 108 Simard, L., Koo, D. C., Faber, S. M., Sarajedini, V. L., Vogt, N. P.,

Phillips, A. C., Gebhardt, K., Illingworth, G. D., & Wu, K. L. 1999, ApJ, 519, 563
Simard et al. 2002, ApJ, in preparation.
Stetson, P. B. 1987, PASP, 99, 191

Tran, K.-V., Simard, L., Zabludoff, A., & Mulchaey, J. 2001, ApJ, 549, 172

Valentijn, E. A. 1990, Nature, 346, 153 Valentijn, E. A. 1994, MNRAS, 266, 614

Valentijn, E. A. 1994, MNRAS, 266, 614
van den Bergh, S. 1960a, ApJ, 131, 215
van den Bergh, S. 1960b, ApJ, 131, 558
van den Bergh, S. 1976, ApJ, 206, 883
Vanderbilt, D., & Louie, S.G. 1984, Journal of Computational Physics, 56, 259
Vogt et al. 2002, ApJ, in preparation.
Watanabe, M., Kodaira, K., & Okamura, S. 1985, ApJ, 292, 72
Wu, K. L. 1999, Ph. D. Thesis, University of California - Santa Cruz Cruz

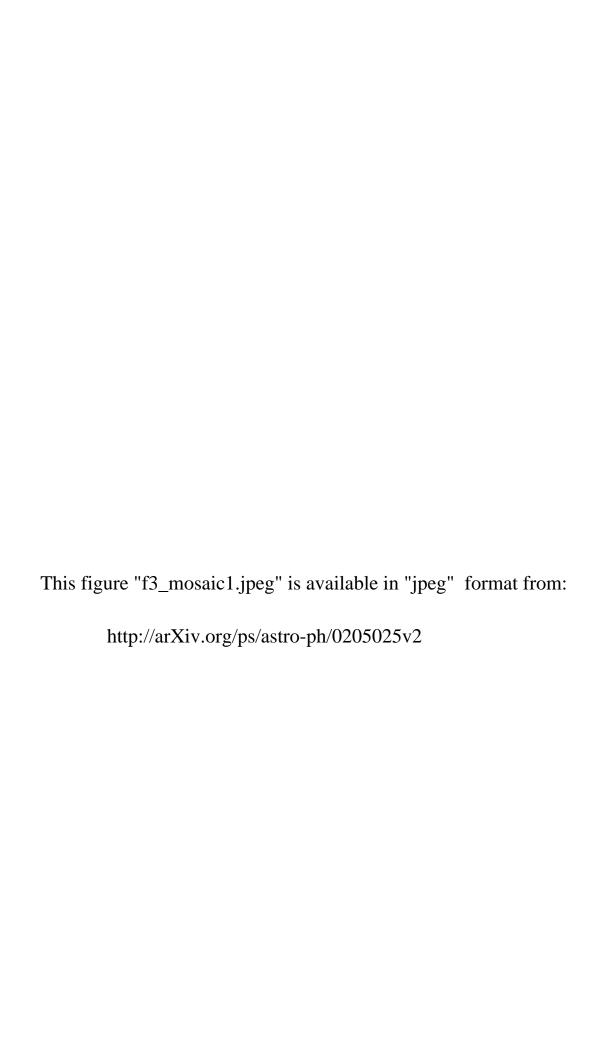
- Fig. 1.— HST/WFPC2/F814W image of the Groth Survey Strip Field 8/Wide Field Camera Chip 3. Image scale is 0.11 pixel<sup>-1</sup>, and the total exposure time is 4400 seconds.
- Fig. 2.— SExtractor segmentation image of GSS image in Figure 1. Every pixel in this image was assigned the non-zero SExtractor flag value of its parent object or a flag value of zero if it was a background pixel. GIM2D uses this segmentation image to independently fit objects which are very close to each other.
- FIG. 3.— Mosaics of GSS thumbnail images drawn at random from the DEEP/GSS sample. The extracted region for each galaxy is twenty times the area of its  $1.5-\sigma_{bkg}$  isophote. First mosaic Science thumbnail images: The numbers shown around each science thumbnail image are the DEEP/GSS object ID (top left), DEEP Keck redshift (top right), observed galaxy total magnitude  $I_{814}$  (bottom left) and observed galaxy  $V_{606}-I_{814}$  color (bottom right). Second mosaic Output PSF-convolved GIM2D model thumbnail images: The numbers shown around each model thumbnail image are the DEEP/GSS object ID (top left), bulge fraction B/T (top right), rest-frame B-band galaxy total absolute magnitude (bottom left), and galaxy log half-light radius in arcseconds (bottom right). Third mosaic Residual thumbnail images (science model): Numbers shown around each residual thumbnail image are the DEEP/GSS ID (top left), RT3 + RA3 asymmetry parameter (top right), concentration index C (bottom left) and asymmetry index A (bottom right). The same greyscale was used for the science, model and residual thumbnail images of a given galaxy, but a different greyscale was used for each galaxy. The bottom greyscale value for each galaxy was set to be  $5-\sigma_{bkg}$  below the science thumbnail background level, and the top greyscale value was set to be  $10-\sigma_{bkg}$  above the background. Notice the close galaxy pair  $192\_2330$  which was successfully deblended by SEXtractor and independently fitted by GIM2D. Also notice the wealth of interesting structures in all the residual images.
- Fig. 4.— Two-dimensional maps of systematic and random galaxy magnitude errors from 5995 DEEP/GSS separate structural fit simulations. Top left-hand panel: Systematic error on recovered galaxy total magnitude  $I_{814,rec}$  as a function of input galaxy log half-light radius  $r_{hl,input}$  in arcseconds and input galaxy total magnitude  $I_{814,input}$ . The top number in each cell is the mean magnitude error  $(I_{814,rec} I_{814,input})$ , and the bottom number is the number of simulations created in that cell. Top right-hand panel:  $1-\sigma$  random error on  $I_{814,rec} I_{814,input}$ ) as a function of  $I_{814,rec}$  and  $I_{814,input}$ . Bottom left-hand panel: Systematic error on  $I_{814,rec}$  as a function of recovered galaxy log half-light radius  $r_{hl,rec}$  in arcseconds and  $I_{814,rec}$ . Bottom right-hand panel: Actual DEEP/GSS  $I_{814,obs}$ -log  $r_{hl,obs}$  observations. Since recovered quantities are the simulation equivalent of the observed ones, this panel should be directly compared to the bottom left-hand panel to see how important magnitude errors are in different regions of the observational magnitude-size plane. Although such 2D maps can be very useful tools, one should keep in mind that they are only two-dimensional projections of a complex multi-dimensional error function.
  - Fig. 5.— Same as Figure 4 except that log half-light radius errors are shown here.
  - Fig. 6.— Same as Figure 4 except that bulge fraction errors are shown here.
- FIG. 7.— Two-dimensional maps of systematic and random galaxy bulge fraction errors from DEEP/GSS separate structural fit simulations with input galaxy half-light radius  $r_{hl,input} \geq 0$ ."1. Top left-hand panel: Systematic error on recovered galaxy bulge fraction  $(B/T)_{rec}$  as a function of input galaxy bulge fraction  $(B/T)_{input}$  and input galaxy total magnitude  $I_{814,input}$ . The top number in each cell is the mean bulge fraction error  $((B/T)_{rec} (B/T)_{input})$ , and the bottom number is the number of simulations created in that cell. Top right-hand panel: 1- $\sigma$  random error on  $(B/T)_{rec}$  ( $\sigma((B/T)_{rec} (B/T)_{input})$ ) as a function of  $(B/T)_{input}$  and  $I_{814,input}$ . Bottom left-hand panel: Systematic error on  $(B/T)_{rec}$  as a function of  $(B/T)_{rec}$  and  $I_{814,rec}$ . Bottom right-hand panel: Actual DEEP/GSS  $(B/T)_{obs}$ - $I_{814,obs}$  observations. Since recovered quantities are the simulation equivalent of the observed ones, this panel should be directly compared to the bottom left-hand panel to see how important bulge fraction errors are in different regions of the observational magnitude-bulge fraction plane.
- Fig. 8.— Two-dimensional maps of systematic and random galaxy magnitude errors from 5195 DEEP/GSS simultaneous structural fit simulations. Top left-hand panel: Systematic error on recovered galaxy total magnitude  $I_{814,rec}$  as a function of input galaxy log half-light radius  $r_{hl,input}$  in arcseconds and input galaxy total magnitude  $I_{814,input}$ . The top number in each cell is the mean magnitude error on  $I_{814,rec} I_{814,input}$ ), and the bottom number is the number of simulations created in that cell. Top right-hand panel:  $1-\sigma$  random error on  $I_{814,rec} I_{814,input}$ ) as a function of  $1-\sigma$  random error on  $1-\sigma$  random error on  $1-\sigma$  random error of recovered galaxy log half-light radius  $1-\sigma$  radius  $1-\sigma$  random error except galaxy log half-light radius  $1-\sigma$  radius  $1-\sigma$  random error er
  - Fig. 9.— Same as Figure 8 except that log half-light radius errors are shown here.
  - Fig. 10.— Same as Figure 8 except that bulge fraction errors are shown here.
- Fig. 11.— Structural component colors recovered by GIM2D from simultaneous structural fit simulations. Top three panels: Recovered galaxy  $V_{606}-I_{814}$  color versus input galaxy  $V_{606}-I_{814}$  color for input galaxy total magnitudes in the ranges  $20.0 \le I_{814} < 21.0$ ,  $21.0 \le I_{814} < 22.0$ , and  $22.0 \le I_{814} < 23.5$ . The mean and rms color differences (recovered—input) are (0.002, 0.020), (0.010, 0.034), and (0.063, 0.087) for the three ranges respectively.  $V_{606,lim}=26.0$ . Middle three panels: Recovered bulge  $V_{606}-I_{814}$  color versus input bulge  $V_{606}-I_{814}$  color for input bulge magnitudes in the ranges  $20.0 \le I_{814}$  (bulge)  $< 21.0, 21.0 \le I_{814}$  (bulge) < 22.0, and  $22.0 \le I_{814}$  (bulge) < 23.5. The mean and rms bulge color differences (recovered—input) are (-0.001, 0.255), (0.022, 0.120), and (0.034, 0.186) for the three ranges respectively.  $V_{606,lim}$  (bulge)  $= 26.0, r_{hl,814} \ge 0$ ."15, and  $r_{hl,606} \ge 0$ ."15. Bottom three panels: Recovered disk  $V_{606}-I_{814}$  color versus input disk  $V_{606}-I_{814}$  color for input disk magnitudes in the ranges  $20.0 \le I_{814}$  (disk)  $< 21.0, 21.0 \le I_{814}$  (disk) < 22.0, and  $22.0 \le I_{814}$  (disk) < 23.5. The mean and rms disk color differences (recovered—input) are (0.008, 0.047), (0.006, 0.211), and (0.030, 0.304) for the three ranges respectively.  $V_{606,lim}$  (disk)  $= 26.0, r_{hl,814} \ge 0$ ."15, and  $r_{hl,606} \ge 0$ ."15.
- Fig. 12.— Two-dimensional maps of systematic galaxy bulge fraction errors from DEEP/GSS separate and simultaneous structural fit simulations as a function of input galaxy bulge fraction and input bulge effective radius/disk scale length ratio. Left-hand panel: Systematic error on recovered galaxy bulge fraction  $(B/T)_{rec}$  from separate structural fits (SPF) as a function of input galaxy bulge fraction  $(B/T)_{input}$  and input log bulge effective radius/disk scale length ratio  $r_e/r_d$ . The top number in each cell is the mean bulge fraction error  $((B/T)_{rec} (B/T)_{input})$ , the middle number in each cell is the minimum error, and the bottom number in each cell is the maximum error. Right-hand panel: Same as left-hand panel but for simultaneous structural fits. These maps show that there do not seem to be any regions where GIM2D can systematically mistake disks for bulges and vice versa.
- Fig. 13.— Median systematic errors on recovered bulge fraction B/T and galaxy total apparent magnitude  $I_{814}$  as a function of asymmetric flux fraction  $f_{HII}$ . Top six panels: Median B/T systematic error in six different magnitude-size ranges. Bottom six panels: Median  $I_{814}$  systematic error in six different magnitude-size ranges. Vertical error bars are 68% lower and upper bounds.

- Fig. 14.— Top six panels: Median systematic error on recovered galaxy log half-light radius  $r_{hl}$  as a function of asymmetric flux fraction  $f_{HII}$  in six different magnitude-size ranges. Vertical error bars are 68% lower and upper bounds. Bottom six panels: Median recovered  $R_A + R_T$  asymmetry index values as a function of asymmetric flux fraction  $f_{HII}$  in six different magnitude-size ranges. Vertical error bars are 68% lower and upper bounds.
- Fig. 15.— Six one-dimensional projections of the photometric selection function  $S_{UP}(\overline{\mathbf{w}})$ : galaxy total apparent magnitude  $I_{814}$  (top left), galaxy bulge fraction (B/T) (top middle), bulge effective radius  $r_e$  in arcseconds (top right), bulge ellipticity e (bottom left), disk scale length  $r_d$  in arcseconds (bottom middle), and disk inclination angle i (bottom right). Filled circles are simulated galaxies with  $0.0 \le (B/T) \le 0.2$ , pluses are galaxies with  $0.2 < (B/T) \le 0.8$ , and triangles are galaxies with  $0.8 < (B/T) \le 1.0$ .
- Fig. 16.— Comparison between MDS and GIM2D parameters for Groth Strip galaxies. Top left: GIM2D versus MDS total galaxy model  $I_{814}$  magnitudes. Top right: GIM2D versus MDS galaxy semi-major axis log half-light radiii in arcseconds for galaxies with  $I_{814} \leq 22$ . Lower left: GIM2D versus MDS galaxy bulge fractions for galaxies with  $I_{814} \leq 22$ . Filled circles are galaxies with  $|I_{814,GIM2D} I_{814,MDS}| \leq 0.2$ , and open circles are the remainder of the sample. The long dashed lines in all three panels are one-to-one lines.

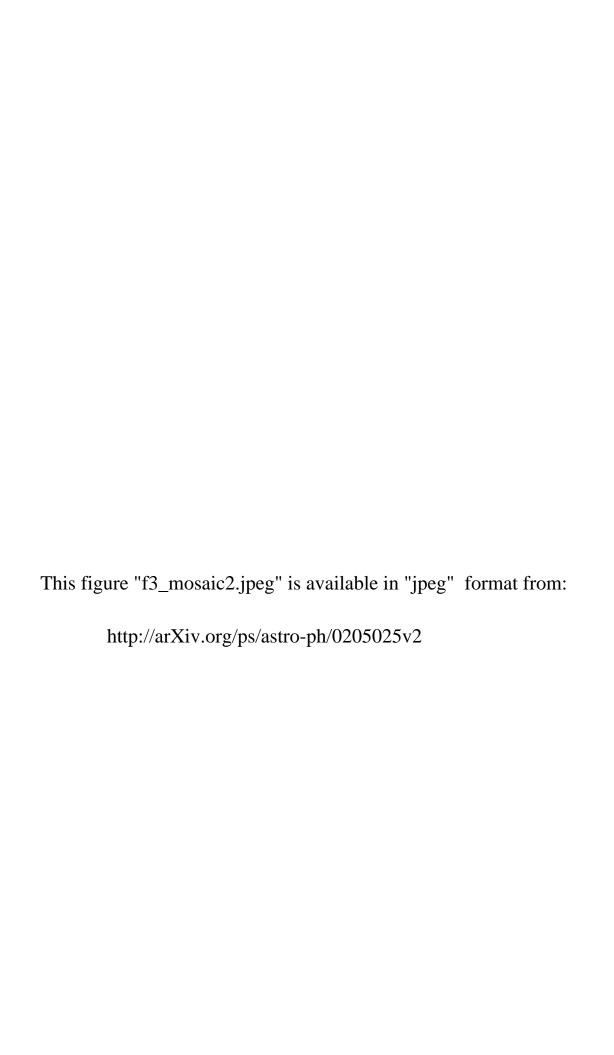
 $\begin{array}{c} {\rm TABLE~1} \\ {\rm HST/WFPC2/GSS~Image~Datasets} \end{array}$ 

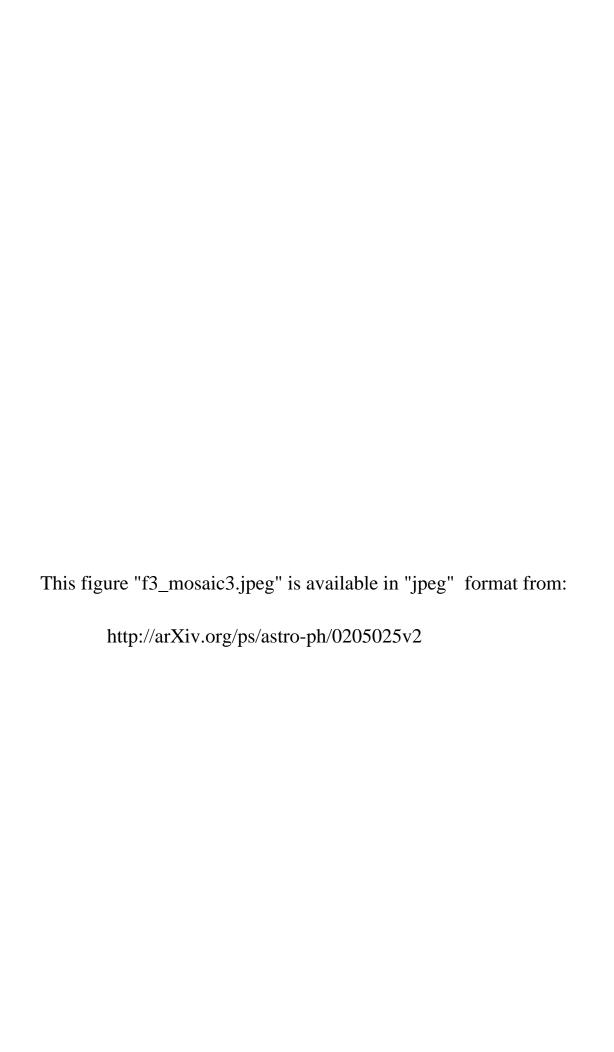
| DEEP/GSS<br>Field ID | HST Target<br>Name  | $^{\alpha}_{(\mathrm{J2000.0})}$ | $^{\delta}_{(J2000.0)}$ | Observation<br>Date | PI                     | MDS<br>Field ID |
|----------------------|---------------------|----------------------------------|-------------------------|---------------------|------------------------|-----------------|
| 4                    | FIELD-141803+523    | 14:18:03                         | +52:32:10               | 16 March 1994       | Groth                  | u26x4           |
| 5                    | FIELD-141757+523    | 14:17:56                         | +52:31:00               | 11 March 1994       | $\operatorname{Groth}$ | u26x5           |
| 6                    | FIELD-141750+522    | 14:17:50                         | +52:29:51               | 13 March 1994       | $\operatorname{Groth}$ | u26x6           |
| 7                    | DEEP-SURVEY FIELD-2 | 14:17:43                         | +52:28:41               | 22 March 1994       | Westphal               | u2ay1           |
| 8                    | FIELD-141737+522    | 14:17:37                         | +52:27:31               | 10 March 1994       | $\operatorname{Groth}$ | u26x7           |
| 9                    | FIELD-141731+522    | 14:17:30                         | +52:26:21               | 11 March 1994       | $\operatorname{Groth}$ | u26x8           |
| 10                   | FIELD-141724+522    | 14:17:24                         | +52:25:11               | 16 March 1994       | $\operatorname{Groth}$ | u26x9           |
| 11                   | FIELD-141717+522    | 14:17:17                         | +52:24:01               | 07 March 1994       | $\operatorname{Groth}$ | u26xa           |
| 12                   | FIELD-141711+522    | 14:17:10                         | +52:22:51               | 07 March 1994       | $\operatorname{Groth}$ | u26xb           |
| 13                   | FIELD-141704+522    | 14:17:04                         | +52:21:41               | 10 March 1994       | $\operatorname{Groth}$ | u26xc           |
| 14                   | FIELD-141658+522    | 14:16:57                         | +52:20:31               | 13 March 1994       | $\operatorname{Groth}$ | u26xd           |
| 15                   | FIELD-141651+521    | 14:16:51                         | +52:19:22               | 16 March 1994       | $\operatorname{Groth}$ | u26xe           |
| 16                   | FIELD-141645+521    | 14:16:44                         | +52:18:11               | 17 March 1994       | $\operatorname{Groth}$ | u26xf           |
| 17                   | FIELD-141638+521    | 14:16:38                         | +52:17:01               | 14 March 1994       | $\operatorname{Groth}$ | u26xg           |
| 18                   | FIELD-141632+521    | 14:16:31                         | +52:15:51               | 16 March 1994       | $\operatorname{Groth}$ | u26xh           |
| 19                   | FIELD-141626+521    | 14:16:25                         | +52:14:41               | 17 March 1994       | $\operatorname{Groth}$ | u26xi           |
| 20                   | FIELD-141619+521    | 14:16:19                         | +52:13:31               | 10 March 1994       | $\operatorname{Groth}$ | u26xj           |
| 21                   | FIELD-141613+521    | 14:16:12                         | +52:12:21               | 09 March 1994       | $\operatorname{Groth}$ | u26xk           |
| 22                   | FIELD-141606+521    | 14:16:06                         | +52:11:11               | 17 March 1994       | $\operatorname{Groth}$ | u26xl           |
| 23                   | FIELD-141600+521    | 14:15:59                         | +52:10:01               | 09 March 1994       | $\operatorname{Groth}$ | u26xm           |
| 24                   | FIELD-141553+520    | 14:15:53                         | +52:08:51               | 15 March 1994       | $\operatorname{Groth}$ | u26xn           |
| 25                   | FIELD-141547+520    | 14:15:46                         | +52:07:40               | 09 April 1994       | $\operatorname{Groth}$ | u26xo           |
| 26                   | FIELD-141540+520    | 14:15:40                         | +52:06:30               | 08 March 1994       | $\operatorname{Groth}$ | u26xp           |
| 27                   | FIELD-141534+520    | 14:15:33                         | +52:05:20               | 08 March 1994       | $\operatorname{Groth}$ | u26xq           |
| 28                   | FIELD-141527+520    | 14:15:27                         | +52:04:10               | 08 March 1994       | $\operatorname{Groth}$ | u26xr           |
| 29                   | FIELD-141823+523    | 14:15:21                         | +52:02:59               | 15 March 1994       | $\operatorname{Groth}$ | u26x1           |
| 30                   | FIELD-141816+523    | 14:15:14                         | +52:01:49               | 15 March 1994       | $\operatorname{Groth}$ | u26x2           |
| 31                   | FIELD-141810+523    | 14:15:08                         | +52:00:39               | 02 April 1994       | Groth                  | u26x3           |

This figure "f1.jpeg" is available in "jpeg" format from:



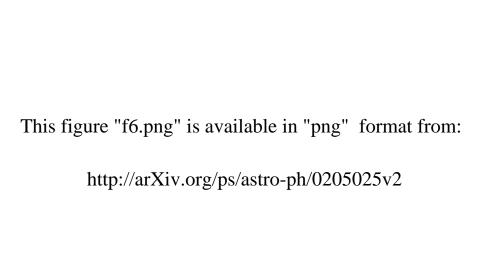
This figure "f2.jpeg" is available in "jpeg" format from:



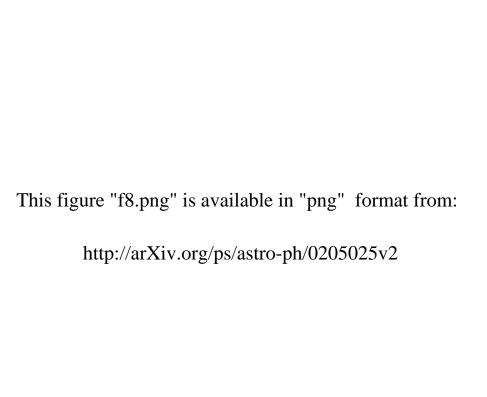


This figure "f4.png" is available in "png" format from:

This figure "f5.png" is available in "png" format from:



This figure "f7.png" is available in "png" format from:



This figure "f9.png" is available in "png" format from:

This figure "f10.png" is available in "png" format from:

This figure "f11.png" is available in "png" format from:

This figure "f12.png" is available in "png" format from:

This figure "f13.png" is available in "png" format from:

This figure "f14.png" is available in "png" format from:

This figure "f15.png" is available in "png" format from:

This figure "f16.png" is available in "png" format from: